

Univerzita Karlova v Praze
Matematicko-fyzikální fakulta

DISERTAČNÍ PRÁCE



Michael Komm

Studium okrajového plazmatu Tokamaku a jeho interakce s první stěnou

Katedra fyziky povrchů a plazmatu

Vedoucí disertační práce: doc. Mg. Pavel Kudrna, Dr.

Konzultant: Dr. Renaud Dejarnac

Studijní program: Fyzika

Studijní obor: Fyzika plazmatu a ionizovaných prostředí

Praha 2011

In questions of science, the authority of a thousand is not worth the humble reasoning of a single individual.

Galileo Galilei

Prohlašuji, že jsem tuto disertační práci vypracoval samostatně a výhradně s použitím citovaných pramenů, literatury a dalších odborných zdrojů.

Beru na vědomí, že se na moji práci vztahují práva a povinnosti vyplývající ze zákona č. 121/2000 Sb., autorského zákona v platném znění, zejména skutečnost, že Univerzita Karlova v Praze má právo na uzavření licenční smlouvy o užití této práce jako školního díla podle §60 odst. 1 autorského zákona.

V dne

Podpis autora

Název práce: Studium okrajového plazmatu Tokamaku a jeho interakce s první stěnou

Autor: Michael Komm

Katedra: Katedra fyziky povrchů a plazmatu

Vedoucí disertační práce: doc. Mg. Pavel Kudrna, Dr. KFPP

Konzultant: Dr. Renaud Dejarnac, IPP CAS CR

Abstrakt: Tato práce představuje výsledky simulací zaměřených na problematiku jaderné fúze za použití Particle-in-Cell kódů SPICE2 a SPICE3. Díky těmto simulacím jsme byli schopni předpovědět toky tepla dopadající z plazmatu na desky divertoru, což je jeden z klíčových problémů budoucích fúzních zařízení. Výsledky simulací také přispěly k pochopení procesu zadržování tritia ve štěrbinách mezi deskami divertoru. Dále jsme byli schopni vysvětlit princip fungování Katsumata sondy.

Klíčová slova: Tokamak, PIC, divertor, tritium, Katsumata

Title: Studies of tokamak edge plasma and its interaction with the first wall

Author: Michael Komm

Department: Department of Surface and Plasma Science

Thesis director: doc. Mg. Pavel Kudrna, Dr. KFPP

Thesis supervisor: Dr. Renaud Dejarnac, IPP CAS CR

Abstract: This work presents results of simulations of nuclear fusion related problems, using both 2D PIC code (SPICE2) and full 3D code (SPICE3). The simulations allowed us to predict particle and heat loads coming from plasma onto the divertor tiles, which is a key problem for the next-step devices. The results of simulations contributed to the research of fuel retention in the gaps between divertor tiles. We were also able to explain the behaviour of the Katsumata probe and verify the validity of its measurements.

Keywords: Tokamak, PIC, divertor, tritium, Katsumata

Contents

1	Introduction	3
1.1	Fusion Energy	3
1.2	Plasma facing components	5
1.3	Fuel retention	7
1.4	Specific issues related to plasma-wall interaction	10
1.4.1	Investigation of plasma interaction with the gaps	10
1.4.2	Ion temperature measurements	11
2	Theory	13
2.1	Edge plasma physics	13
2.1.1	Plasma sheath	13
2.1.2	Chodura sheath	15
2.1.3	Motion of particles in the magnetic sheath	17
2.2	Introduction to plasma modeling	20
2.2.1	Fluid modeling	20
2.2.2	Vlasov equation modeling	20
2.2.3	Particle-In-Cell modeling	21
2.2.4	Gyro-kinetic modeling	22
3	Motivation of the thesis	25
4	SPICE2 code	27
4.1	Programming environment	28
4.2	Normalization	28
4.3	Particle injection	29
4.4	Equation of motion	31
4.5	Weighting	31
4.6	Poisson solver	31
4.7	Boundary Conditions	33
4.8	Parallelization	34
4.8.1	Particle decomposition	34

4.8.2	Domain decomposition	34
4.9	I/O files	37
5	Simulations of the TEXTOR tiles	39
5.1	Introduction	39
5.2	SPICE2 setup	39
5.3	Results of simulations	40
5.3.1	Unshaped gaps	40
5.3.2	Shaped gaps	47
5.4	Summary of the TEXTOR simulations	50
6	Simulations of the Katsumata probe	53
6.1	SPICE3 - description	53
6.1.1	Poisson solver	53
6.1.2	Simulation limits	55
6.2	Simulations of the Katsumata Probe	56
6.2.1	Geometry of the probe model	57
6.2.2	Simulation scenario	58
6.3	Electron transport inside the tube	58
6.3.1	Ion temperature estimation	60
6.4	Mechanism of electron shielding	61
6.4.1	Role of magnetic field inclination	61
6.5	Summary of the Katsumata probe simulations	62
7	Simulations of gap crossings	63
7.1	Introduction	63
7.2	Geometry of the simulations	63
7.3	Results of simulations	65
7.4	Maximum of the power flux	67
7.5	Summary of the 3D simulations of gap crossings	70
8	General conclusions	73

Chapter 1

Introduction

1.1 Fusion Energy

As the world population continues to grow and industry production increases, the question of suitable energy sources becomes more and more a topic of interest. The current main sources (coal, oil and nuclear fission) are all rather limited [1], although the estimates of their reserves vary widely. In addition, their resources are localized, which creates political dependencies and tensions between countries. For these reasons, there is an intensive ongoing research in the field of alternative energy sources.

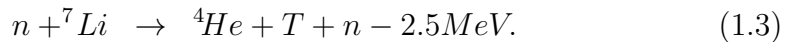
One possibility is to use renewable sources, which usually include water, wind, solar, tidal and geothermal power stations. These sources do not require any fuel in the conventional meaning, however, their energy production is not stable but fluctuates with natural conditions. The problem of energy storage on a large scale is still unresolved, and so these sources are not suitable for industry and other applications, which require constant power supply.

A candidate for a source with abundant fuel and sufficient reserves for a long period of time is nuclear fusion. Unlike fission, where a heavy nucleus is being split into lighter parts, a process which is accompanied by energy release, in fusion, light nuclei are fused into a heavier one, to produce a large amount of energy (of order 10^6 times more than in chemical reactions). Since all nuclei have positive charge, a strong force is needed to push nuclei close together, so that fusion can occur. In stars, this force is the gravitation, here on Earth other approaches have to be studied. The most promising way to achieve fusion is to keep thermalized fusion fuel in the plasma state at high density for long enough time, so that collisions between plasma particles result in fusion. The suitable temperature of plasma is governed by the

effective cross-section of each fusion reaction, the plasma density and critical time are related by the *Lawson criterion* [2]. The reaction with highest reaction rate [3], which is currently intended to be used in the first generation of fusion reactors is the following:



The reactants here are isotopes of hydrogen - deuterium, which is stable and widespread in water, and tritium, which is radioactive and almost inexistent on Earth naturally. Tritium can be produced inside the plant by bombardment of a lithium blanket with the neutrons from fusion reactions. This is called tritium breeding



Lithium can be extracted from soil. The estimates of resource reserves state that there is sufficient deuterium and lithium on Earth to cover at least 10^7 years of world energy consumption. The reaction 1.1 does not require transportation of radioactive elements (tritium will be produced inside the plant) and does not produce direct radioactive waste. However, some parts of the reactor will get activated by the high energy neutrons coming from fusion reactions. This activation can be reduced by a choice of suitable materials and in total is much less problematic than in standard fission reactors. Unlike fission, there is no chain reaction involved and the conditions for fusion are extremely difficult to achieve and so the risk of uncontrolled reactions is negligible.

Although there is number of possible fusion concepts, which are a subject of an intensive research, the tokamaks are considered as the most advanced approach. The largest current european fusion device, JET (Joint European Torus) [4], is of tokamak type and so will be the forecoming ITER (International Thermonuclear Experimental Reactor) machine [5]. The plasma in tokamak is magnetically confined in a toroidally shaped vacuum vessel. Schematic view of a tokamak device is shown in Fig. 1.1. The *toroidal* direction follows the center of the torus (and also the plasma current), while the *poloidal* direction wraps around the plasma cross-section. The toroidal magnetic field is produced by coils, while the poloidal field is created by the plasma current. This combined magnetic field reduces radial particle and energy losses and at the same time plasma current heats up the plasma. Tokamaks work as transformers, where the plasma serves as its secondary winding. The plasma current is driven by induction and as such, tokamaks

were originally designed as short-pulsed devices with discharges lasting few seconds at maximum. Later, non-inductive means of current drive were discovered and with the help of supraconducting coils today some tokamaks are capable of discharges several minutes long.

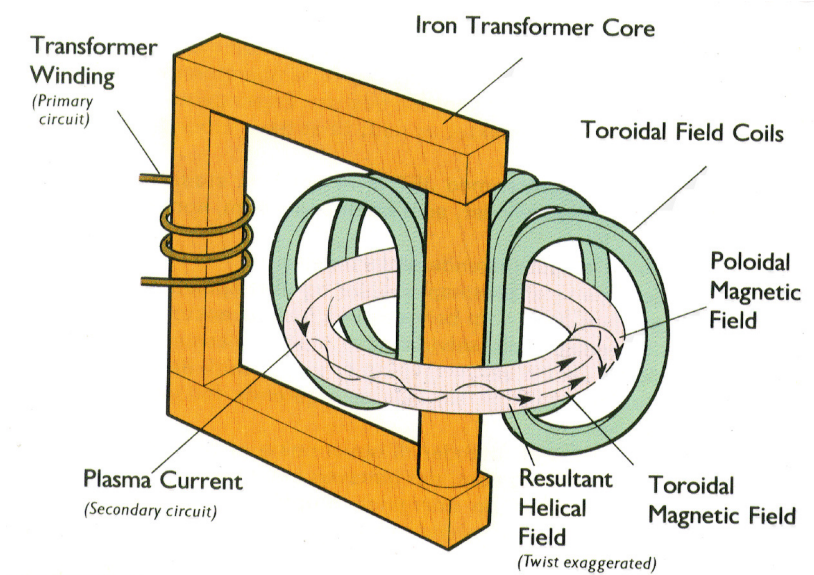


Figure 1.1: Main components and directions in tokamak.

Tokamak dimensions can be briefly described by two main parameters - the major radius R_0 and minor radius a as shown in Fig. 1.2 The radii have been increasing throughout the history of fusion research, the summary of of tokamaks mentioned in this work is in table 1.1. Apart from the major and minor radius, the plasma current I_p and toroidal magnetic field B_T are shown.

1.2 Plasma facing components

As described in the previous section, in order to achieve conditions suitable for fusion, it is necessary to keep plasma at very high temperatures and well separated from the walls of the vacuum vessel. Any contact of hot plasma with the solid material leads to destructive processes and emission of eroded materials into the plasma, which can work as a energy loss channel via cyclic ionization and recombination. Even the sophisticated toroidal configuration with twisted magnetic field lines does not result in perfect confinement -

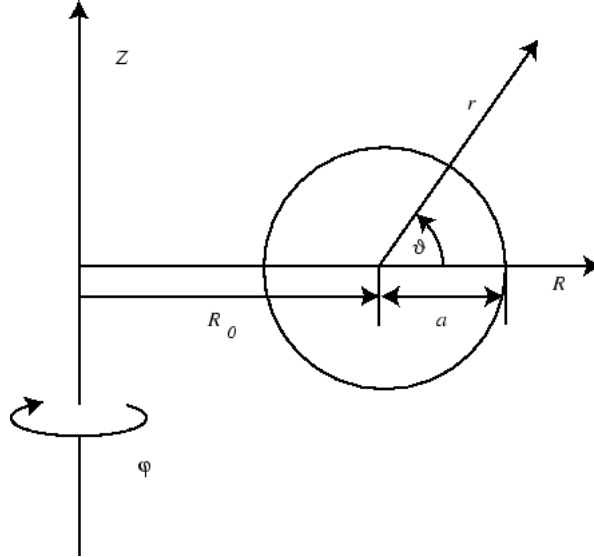


Figure 1.2: Toroidal coordinates showing the major radius R_0 and the minor radius a of a tokamak.

Tokamak	R_0 [m]	a [m]	I_p [MA]	B_T [T]
GOLEM [6]	0.4	0.09	0.025	1.5
COMPASS [7]	0.56	0.21	0.32	2.1
TEXTOR [8]	1.75	0.47	0.8	2.8
ASDEX-U [9]	1.65	0.8	1.4	3.9
TORE-SUPRA [10]	2.25	0.7	2.0	4.5
DIII-D [11]	1.66	0.67	3.0	2.2
JET [4]	2.96	0.96	6.0	4.0
ITER [5]	6.2	2.0	15.0	5.3

Table 1.1: List of selected contemporary tokamaks with their main parameters: major radius R_0 , minor radius a , plasma current I_p and toroidal magnetic field B_T .

processes like collisions or various instabilities create a cross-field transport towards the walls of the system [12]. It is therefore necessary to form special parts of the vessel, which will (1) withstand the contact with the plasma and (2) minimize the plasma pollution.

Originally, the poloidal cross section of the tokamak plasma was circular and so were the nested flux surfaces. The size of the plasma was limited by a wall component called *limiter* as shown in Fig. 1.3. The closed flux surface with the largest radius is called *Last Closed Flux Surface* (LCFS). Magnetic surfaces outside the LCFS were intercepting the limiter. This configuration is not optimal for high confinement since the LCFS is in contact with a solid material and so the impurities spread easily into the core plasma. Nevertheless, the limiter configuration is still used in tokamaks in operation (e.g. TEXTOR, Tore Supra, GOLEM).

In order to minimize the amount of impurities inside the confined region, it was necessary to separate the LCFS from the wall by a certain distance. This can be achieved by forming the LCFS entirely by magnetic fields, in the *divertor* configuration. Driving a current in an extra poloidal coil creates a point with zero magnetic field (x-point) and the open field lines are deflected to the neutralizer plates far from the confined plasma. Tokamaks with divertors can reach the high confinement mode (H-mode) more easily than traditional limiter-equipped devices. The H-mode leads to better confinement but also brings new difficulties, mainly MHD instabilities called Edge Localized Modes (ELMs). There are various types of ELMs but in general they represent sudden bursts of plasma at high temperatures and densities towards the wall. The amount of energy transferred during one ELM towards the wall can be significant (up to 10% of the total energy) and cause severe damage to plasma facing components. Divertor and limiter plates have typically low inclination angle with respect to the B field lines, which allows to spread the heat load over a larger surface.

1.3 Fuel retention

Future fusion reactors will be using D-T mixture as a fuel. While the physical properties of deuterium are practically the same as of hydrogen, tritium is an unstable isotope, a weak β emitter with a half-time of 12.3 years. It behaves chemically in the same way as hydrogen, so it can be easily bound in water (HTO) or in various hydrocarbons. As such, it can easily penetrate into living organisms, increasing the destructive power of β radiation. The biological half-time of tritium in human body is roughly 10 days. There are several safety regulations concerning the manipulation with tritium to ensure the safe

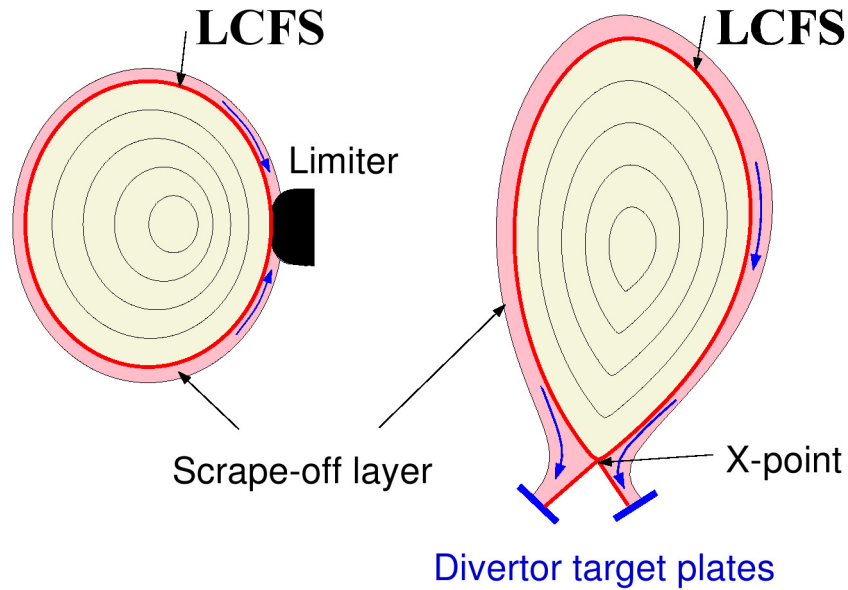


Figure 1.3: Different approaches towards the LCFS formation.

operation of the reactor. One of them restricts the amount of tritium that can be contained in the vacuum chamber. This limit reads 700 g of tritium for the ITER device. Given that the amount of tritium in the plasma for each discharge is supposed to be in order of grams it seems that this regulation will not bring any difficulties. However, a long term research [13] has shown that the fuel has a very strong tendency to get accumulated in the walls of the vacuum vessel and in plasma facing components. So far, most of the fusion experiments have been done with deuterium but the unfortunate properties of tritium are expected to be similar. The fuel retention is a subject of intensive research, the mechanisms of deuterium/tritium accumulation are studied on many tokamaks, such as JET , TEXTOR, TORE SUPRA and DIII-D, or linear devices like PISCES [14]. The amount of fuel retained in the vessel can be studied by different approaches - gas balance (where the amount of pumped fuel is compared to the total injected in a discharge) or post-mortem material analysis of plasma-facing components (PFCs). This leads to rather wide range of estimated retention between 2 - 20% [15]. This amount depends mainly on the material of PFCs and its temperature during discharge.

In order to withstand thermal shocks and reduce halo currents, the PFCs have to be *castellated* - split into blocks separated by small gaps (typically 1 mm wide). The gaps are either *toroidal*, i.e. parallel to the direction of

the magnetic field, or *poloidal*, i.e. perpendicular to the field. The depth of the gaps is around 1 cm, the usual size of the tile block. An example of a castellated PFC is shown in Fig. 1.4. Measurements on DIII-D show that up to 40% [16] of retained fuel can be stored in such gaps. More importantly, the gaps are particularly difficult for access by cleaning techniques, which are developed to reduce the fraction of fuel retained inside the vessel.

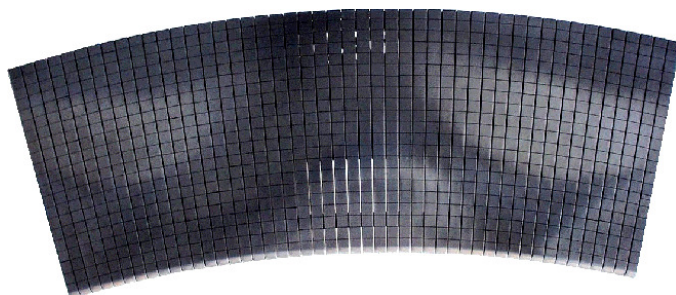


Figure 1.4: Section of the castellated toroidal pumped limiter at Tore-Supra tokamak.

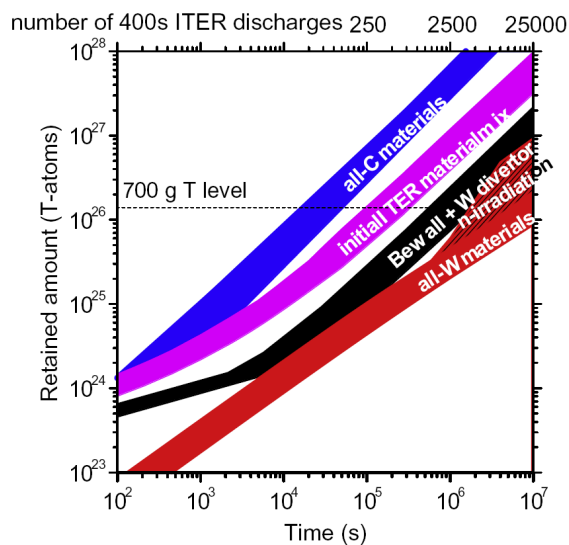


Figure 1.5: Estimated number of allowed ITER discharges for different material combinations [17].

Each wall material has its own mechanisms of retention. Carbon is capable of chemical erosion and formation of deuterium-enabled hydrocarbons

[18]. These hydrocarbons can be deposited in layers and as such do not exhibit any saturation of retention. In case of beryllium and tungsten, chemical erosion does not occur and so the main mechanisms of accumulation is ion implantation and subsequent bulk diffusion [19]. Co-deposition of fuel in layers is still observed in case of beryllium, as there is high sputtering followed by re-deposition. Overall, the level of accumulation is expected to be much lower than in case of carbon, which restricts its use in proposed reactors. Unfortunately, it is rather difficult to achieve high performance discharges in machines with tungsten walls, unless intensive boronization [20] is used [21] to reduce high-Z impurity release into the core plasma. This has important consequences for ITER. In the tritium phase, ITER is planned to operate without carbon, only with a combination of beryllium and tungsten PFCs. However, in the first (hydrogen-deuterium) phase, it will have CFC divertor tiles, which should facilitate initial experimental discharges. The predicted number of ITER discharges before reaching the safety limit of tritium retention for each material combination is shown in Fig. 1.5

1.4 Specific issues related to plasma-wall interaction

1.4.1 Investigation of plasma interaction with the gaps

The physics of plasma behavior in the vicinity of tile gaps is a complicated issue, which is a subject of intensive research on a number of machines. There has been a series of dedicated experiments [22] [23] at the TEXTOR tokamak with the so-called test limiter to study deposition inside gaps of castellated surfaces. The geometry of the limiter is shown in Fig.1.6. This limiter consists of both shaped and non-shaped gaps 0.5 mm wide between rectangular tiles of 10x10 mm². After a sequence of discharges, the test limiter was removed from TEXTOR and analyzed. Results from the post-mortem analysis provide information about the material mixing, erosion and deposition [24] inside gaps but no direct observations of the transport mechanisms. Theoretical modeling of the gaps involves estimation of a number of unknown parameters, which results in only partial agreement with experiment. One of the aims of this work is to improve the theoretical model 3D-GAPS previously developed at Forschungszentrum Jülich [25] in order to study layer formation inside the gaps by providing a realistic plasma particle flux and electrical potential distribution in the vicinity of such complex geometry. These characteristics are calculated by a 2D Particle-In-Cell code SPICE2 [26], which is described in more detail in chapter 4.

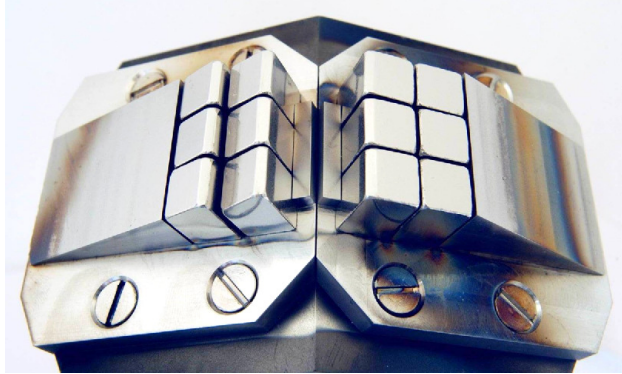


Figure 1.6: Photo of the TEXTOR test limiter with shaped and non-shaped gaps.

The fuel retention is not the only problem connected with gaps. Large machines, such as ITER, will operate with hot and dense plasmas, which can produce enormous heat loads ($q_{\perp} = 80 \text{ MW/m}^2$) when in contact with the PFCs. The tiles have engineering limits at around 10 MW/m^2 in steady state, depending on the material. Should this limit be exceeded, a number of undesired mechanisms (melting, cracking, erosion) [27] can significantly shorten the PFC lifetime. In order to minimize the heat loads, the PFCs are inclined at an oblique angle with respect to the magnetic field, so that the loads spreads over a large surface. However, the poloidal gaps expose tile edges, which are almost perpendicular to the magnetic field and so unacceptable heat loads are expected to occur there. Hotspots can appear especially at the corners of the tiles. A single hot spot on a tile surface can eventually lead to a macroscopic modification of the tile shape and a subsequent destruction of the entire tile.

1.4.2 Ion temperature measurements

The ion temperature T_i is an important plasma quantity. Unlike typical laboratory plasmas, where ions are assumed to be at room temperature, fusion plasmas have T_i similar to T_e . Since most of the heat load is carried by ions, it is necessary to know the T_i in order to estimate the power fluxes. It is not possible to deduce T_i from a simple Langmuir probe current-voltage (I-V) characteristics, due to the collection of large electron current in the ion-repelling regime. Several attempts were made to overcome this issue by various electrostatic probes [28], such as segmented tunnel probe [29], the Retarding Field Analyzer (RFA) [30] or the Katsumata probe [31] [32].

The modeling of the Katsumata probe is a subject of section 6.2. The initial model of the probe relies on a geometrical shielding of a collector submerged inside a metal tube. Since the electrons have small Larmor radii, they should not be able to reach the collector, which is retracted inside the tube by a distance $h \gg r_{Le}$. Ions have Larmor radii comparable to h and as such can reach the collector and contribute to the current measured in the I-V characteristics. This model has been contradicted by an experiment [33], where electron current has been observed even for large h . The shielding is only functional, when the tube (also called *the guard electrode*) is kept at the same potential as the collector during the sweeping. The aim of our probe modeling is to explain this phenomena and provide a more reliable model of the probe.

Chapter 2

Theory

2.1 Edge plasma physics

2.1.1 Plasma sheath

In order to understand the plasma-surface interactions it is necessary to study the plasma behavior in the vicinity of the surface. In general, electrons have higher mobility than ions so their charge flow towards a solid material with plasma would dominate that of ions. This is the reason why all objects in plasma saturate with negative charge (supposing there is no biasing). This charge creates a drop of the plasma potential, called *the sheath*. In equilibrium, the sheath repulses electrons and attracts ions towards the wall so that the net current is zero. The sheath has a typical thickness of several Debye lengths and only a small part of the potential drop called *pre-sheath* extends further into the plasma. For a simple case, ignoring the presence of a magnetic field for a hydrogen plasma without impurities, we can use a one-dimensional model to investigate the sheath. The plasma potential can be calculated using the Poisson equation

$$\frac{d^2\phi}{dx^2} = \frac{e}{\epsilon_0} (n_e - n_i), \quad (2.1)$$

where n_e and n_i are the electron and ion densities, respectively. We assume Boltzmann distribution for electrons so their density is driven by the potential ϕ and electron temperature T_e

$$n_e = n_0 \exp\left(\frac{e\phi}{T_e}\right). \quad (2.2)$$

The ion density can be derived from the conservation of kinetic energy and conservation of flux

$$\frac{1}{2}m_i v_i^2 = \frac{1}{2}m_i v_0^2 - e\phi, \quad (2.3)$$

here v_0 is the velocity of an ion entering the sheath. The ion flux $n_i v_i$ has to be constant everywhere, so the ion density reads

$$n_i = n_0 \left(\frac{\frac{1}{2}m_i v_0^2}{\frac{1}{2}m_i v_0^2 - e\phi} \right)^{1/2}. \quad (2.4)$$

Putting the above density relations into the Poisson equation 2.1 leads to a differential equation for the potential

$$\frac{d^2\phi}{dx^2} = \frac{n_0 e}{\epsilon_0} \left[\exp\frac{e\phi}{T_e} - \left(\frac{\frac{1}{2}m_i v_0^2}{\frac{1}{2}m_i v_0^2 - e\phi} \right)^{1/2} \right]. \quad (2.5)$$

Apparently, the value of v_0 is a critical parameter determining the nature of the solution. We can either obtain an oscillating solution or an exponential decay; the latter agrees with observations. Taking a limit for small ϕ provides

$$\frac{d^2\phi}{dx^2} = \frac{\phi}{\lambda_D^2} \left[1 - \frac{T_e/m_i}{v_0^2} \right]. \quad (2.6)$$

The condition for decaying solution reads

$$v_0 \approx (T_e/m_i)^{1/2}. \quad (2.7)$$

This solution ignores the ion temperature. A more general formula would be

$$v_0 = c_s \approx \left(\frac{T_e + T_i}{m_i} \right)^{1/2}. \quad (2.8)$$

This is an important result - the plasma enters the sheath at the ion sound speed. It resembles the behavior of a neutral gas although the underlying mechanisms are very different.

It is difficult to calculate the exact shape of the sheath but we can easily deduce the total potential drop (which is the most interesting aspect of the sheath). We expect the total current towards the wall to be zero. The ion current density is

$$j_i = n_0 e c_s. \quad (2.9)$$

Boltzmann electrons will have the charge density

$$j_e = -\frac{1}{4}n_0 e (8T_e/\pi m_e)^{1/2} \exp\left(\frac{e\phi_0}{T_e}\right). \quad (2.10)$$

By combining these two equations we can find a solution for ϕ_0

$$-\frac{e\phi_0}{T_e} = \frac{1}{2} \ln \left[\frac{m_i/m_e}{2\pi(1 + T_i/T_e)} \right]. \quad (2.11)$$

The logarithmic expression is not very sensitive to small changes in temperature, the potential drop has a value around 3 for typical edge hydrogenic plasma parameters. This model neglects several effects, the most important being the secondary electron emission. A more general formula (taking into account total secondary emission coefficient δ) is

$$-\frac{e\phi_0}{T_e} = \frac{1}{2} \ln \left[\frac{(1 - \delta^2)m_i/m_e}{2\pi(1 + T_i/T_e)} \right]. \quad (2.12)$$

The coefficient δ can be close to unity and so the secondary emission can significantly affect the sheath. The particle flux towards the wall results in various erosion processes, namely *sputtering*, *desorption* etc. The heat load warms up the wall causing the material to evaporate or even melt. This is an important issue in the design of steady state operation devices. For discharges lasting more than 60 s it is necessary to have actively-cooled plasma facing components. The expected heat load for ITER divertor is approaching the safety limit of 10 MW/m² in steady state and can temporarily exceeded should the off-normal events appear. The sputtered particle flux from the walls is another critical factor limiting the confinement time of the discharge. Therefore the choice of materials and design of the divertor/limiter is a major challenge for engineers.

The power flux to the surface can be expressed as

$$P = n_e c_s T_e \left[\frac{2T_i}{T_e} + \frac{2}{1 - \delta} + \frac{1}{2} \ln \left(\frac{(1 - \delta^2)m_i/m_e}{2\pi(1 + T_i/T_e)} \right) \right]. \quad (2.13)$$

This rather complicated formula can be simplified as

$$P = \gamma_s \Gamma T_e, \quad (2.14)$$

where Γ is the ion flux density and γ_s is called *the heat power transmission factor*, which has a typical value of 6.5 for isothermic hydrogen plasma without secondary emission.

2.1.2 Chodura sheath

Simple model of the sheath described above was premising absence of the magnetic field or a homogeneous magnetic field perpendicular to the surface

(and so without any effect on the model). However, all tokamaks operate under a strong magnetic field and the field lines have usually an oblique angle of a few degrees with respect to the surface. The reason for this is an engineering issue - for envisaged reactor target plasma the parallel heat load would be of order 10^8 Wm^{-2} , i.e. 2 orders of magnitude beyond the material safety limits. It is therefore necessary to spread the load over a larger surface.

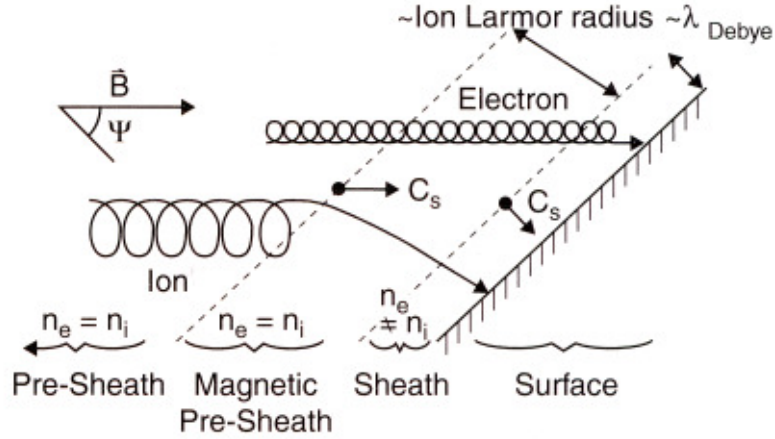


Figure 2.1: Schematical representation of the chodura sheath.

The regular sheath without the magnetic field is characterized by a length of the Debye shielding, the Debye length λ_D

$$\lambda_D = \sqrt{\frac{\epsilon_0 k T_e}{q_e n}} \quad (2.15)$$

The presence of magnetic field at oblique angle to the surface modifies the properties of the pre-sheath and gives rise to a *magnetic pre-sheath* (also known as *Chodura sheath*) [34]. The width of the magnetic pre-sheath is determined by the Larmor radius r_L

$$r_L = \frac{v_{\perp} m}{q B}, \quad (2.16)$$

where m and q is the mass and charge of a given particle and v_{\perp} is the velocity component perpendicular to the direction of magnetic field. In the absence of macroscopic electric fields particles follow a helical trajectory with the radius equal to r_L (as shown later in this section). The plasma in the magnetic pre-sheath is quasineutral but its density decreases towards the

surface. Ions enter the magnetic pre-sheath at their sound speed, which was previously calculated for the regular sheath boundary.

The ratio of the ion Larmor radius and the Debye length determines the nature of the magnetic pre-sheath. For typical tokamak SOL plasma ($n = 10^{19} \text{ m}^{-3}$, $T_e = 20 \text{ eV}$), the Debye length is of the order of 10^{-5} m , while the ion Larmor radius is usually millimetric and so the ratio of the two quantities

$$\xi = \frac{\lambda_D}{r_L} \quad (2.17)$$

is typically in the range of 10 to 100. The graphs in Fig. 2.2 show important features of the magnetic sheath - the Bohm criterion is still fulfilled and ions enter the sheath at their sound speeds. In case, where the ξ would be less than unity, the magnetic pre-sheath vanishes and the sheath behaves as described in the previous section.

2.1.3 Motion of particles in the magnetic sheath

In order to understand the particle motion in the magnetic sheath, we shall start with a simple model of a homogeneous B field $(0, 0, B)$ and perpendicular E field $(0, E_0, 0)$ in the equation of motion:

$$\frac{d\mathbf{v}}{dt} = \frac{q}{m} [\mathbf{E} + (\mathbf{v} \times \mathbf{B})] \quad (2.18)$$

By taking a second derivative of velocity and combining the equations, a second order ODE is obtained:

$$\frac{d^2 v_x}{dt^2} = - \left(\frac{qB}{m} \right)^2 \left(v_x - \frac{E_0}{B} \right) \quad (2.19)$$

$$\frac{d^2 v_y}{dt^2} = - \left(\frac{qB}{m} \right)^2 v_y \quad (2.20)$$

$$\frac{d^2 v_z}{dt^2} = 0 \quad (2.21)$$

The equation for y component yields a standard linear harmonic oscillator (Larmor motion) with the characteristic frequency

$$\omega = \frac{qB}{m}. \quad (2.22)$$

The x component is a linear harmonic oscillator combined with a constant particular solution

$$v_x = v_{\perp} e^{i\omega t} + \frac{E_0}{B} \quad (2.23)$$

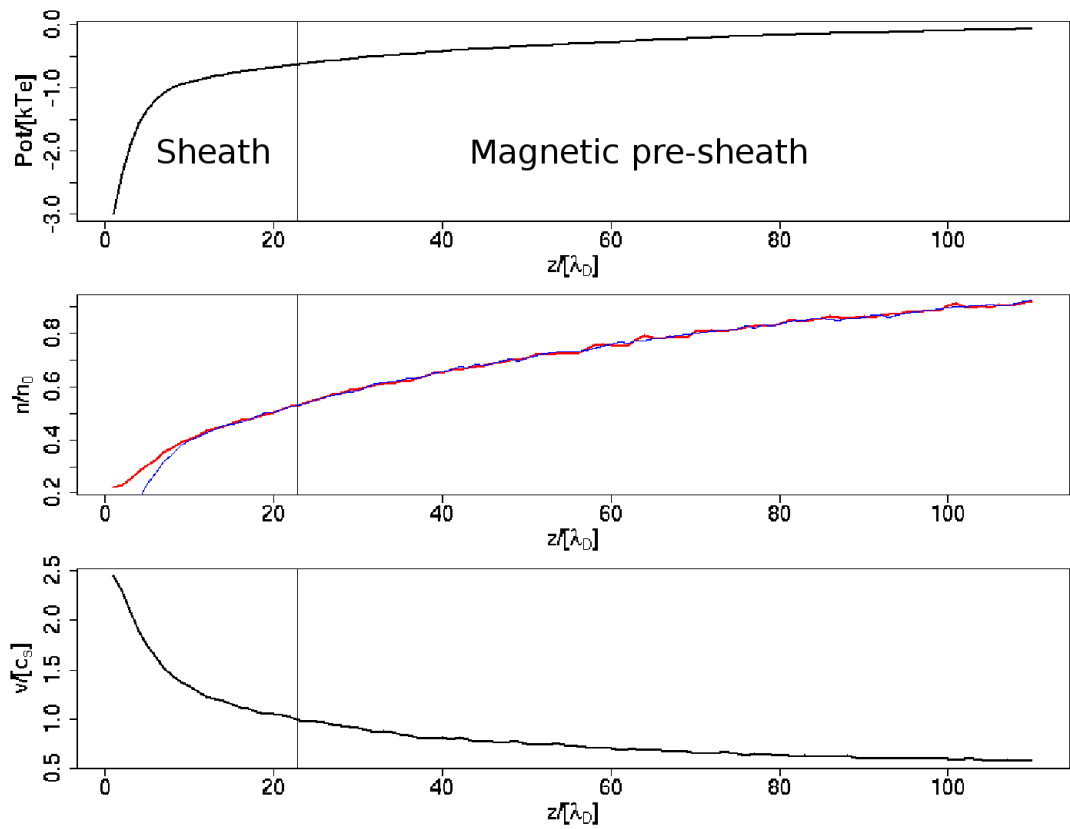


Figure 2.2: Normalized potential and density drop in the magnetic sheath (red ion density, blue electrons), third graph shows increase of the ion velocity normalized to ion sound speed.

which is the $\mathbf{E} \times \mathbf{B}$ drift velocity, perpendicular to the direction of both the electric and magnetic field. The general formula for the drift in homogeneous electric field is

$$v_{E \times B} = \frac{\mathbf{E} \times \mathbf{B}}{B^2} \quad (2.24)$$

The situation becomes different when we introduce spatially varying electric field, which reflects the usual sheath conditions. Lets consider an E field with constant gradient a in the y direction of the surface

$$E_y = E_0 + ay. \quad (2.25)$$

In reality the gradient of the sheath E field varies approximately exponentially towards the surface but the consequences are similar. The differential equation for v_y changes to

$$\frac{d^2 v_y}{dt^2} = \frac{q}{m} \left[a - \frac{q}{m} B^2 \right] v_y, \quad (2.26)$$

which introduces an important limiting condition

$$a > \frac{q}{m} B^2 \quad (2.27)$$

or in more general form

$$\frac{\nabla E}{B} > \omega. \quad (2.28)$$

This equation has two types of solutions, for $a < \frac{q}{m} B^2$ it is the standard oscillatory Larmor motion (though with modified gyro-frequency). For $a > \frac{q}{m} B^2$ the solution is exponential, the Larmor motion breaks. This is called *demagnetization*. This condition is usually fulfilled in narrow regions inside the sheath. In these regions the magnetic force can be neglected and the trajectories of particles can be approximated by motion in a given electrical potential.

Sometimes the effects associated to the Larmor gyration are not important for the plasma behaviour. This is typically the case for electrons, with Larmor radii much smaller than the ion Larmor radius, which determines the properties of the Chodura sheath. In this case, we can apply the *guiding-center approach* and simplify the model of particle's motion. Instead of following the real particle, we should follow its position averaged over the period of the Larmor gyration. By time averaging the solution of equation 2.18 we arrive to the equation of motion for the guiding center, which in the

absence of external forces follows the magnetic field lines. When the external force (electrical force in our case) is applied, the guiding center moves with a drift velocity, as calculated in eq. 2.23.

$$v_x(t) = \frac{E_0}{B} \quad (2.29)$$

$$v_y(t) = 0 \quad (2.30)$$

$$v_z(t) = v_z(t_0) \quad (2.31)$$

The guiding center approach breaks when the particles reach condition 2.28 and their motion is no longer governed by the gyration.

2.2 Introduction to plasma modeling

This section gives a brief introduction into various approaches used in numerical simulations of plasma. Numerical models have been used in plasma research for decades and resulted in a large family of different methods; here only the most important ones are discussed.

2.2.1 Fluid modeling

Given the complicated behavior of hot plasma, it is almost surprising how many situations can be modeled using a simple fluid approximation. These models do not take into account the particle-related properties of plasma but assuming a Maxwellian distribution regarding the plasma as a fluid, continuous quantity. The modeling consists of simultaneous solution of equations relating plasma density, temperature, pressure and electric field. In general, the fluid models (especially those with reduced dimensions) are very fast and allow to model huge volumes of plasma. The main inconvenience is the assumption of quasineutrality and Maxwellian distribution of particle velocities, which are not satisfied in the sheath. That is why fluid models are not suitable for modeling of the sheath.

2.2.2 Vlasov equation modeling

Vlasov (or Fokker-Planck) equation is the basic relation of kinetic theory of plasma. The equation of the particle distribution function f reads

$$\frac{\partial f}{\partial t} + \mathbf{v} \cdot \nabla f + \frac{q}{m} (\mathbf{E} + \mathbf{v} \times \mathbf{B}) \cdot \frac{\partial f}{\partial \mathbf{v}} = \left[\frac{\delta f}{\delta t} \right]_s. \quad (2.32)$$

The solution of this equation is a distribution function varying in time and space. The knowledge of the distribution function allows calculation of the fluid quantities by simple integration, for example:

$$n = \int_{-\infty}^{\infty} f(v)dv, \quad (2.33)$$

$$\Gamma = \int_{-\infty}^{\infty} vf(v)dv, \quad (2.34)$$

The term on the right hand side of eq. 2.32 is the collisional term, which can take many forms depending on the situation. The Vlasov modeling gives more detailed information about plasma behavior and does not have any Maxwellian assumption but still ignores individual particles. The models to solve this equation are in general much slower than fluid models and rather complicated.

2.2.3 Particle-In-Cell modeling

Particle-In-Cell [35] modeling represents the most detailed way of plasma modeling. The trajectory of each particle i is being calculated from its equation of motion

$$\frac{dv_i}{dt} = \frac{q_i}{m_i} (\mathbf{E} + \mathbf{v}_i \times \mathbf{B}). \quad (2.35)$$

In most cases, the magnetic field is externally imposed and the electric field is calculated using the Poisson equation

$$\Delta\phi = -\frac{\rho}{\epsilon_0}, \quad (2.36)$$

$$\mathbf{E} = -\nabla\phi. \quad (2.37)$$

A truly kinetic calculation of fusion plasma would be impossible to perform on present hardware - with typical plasma density of 10^{19} m^{-3} , the model would have to follow 10^{13} particles just to simulate one cubic centimeter of plasma. Therefore a number of speed-up tricks is being used to make the simulation possible while keeping the physical reliability. Instead of calculating the path of every single particle, it is common to calculate the movement of clouds of particles, so called *macroparticles*. The typical number of particles contained in one macroparticle is of the order of $10^6 - 10^7$. In most cases this simplification does not cause any constrains. However, for certain problems (e.g. simulation of a very small plasma current flowing to a surface) artificial oscillations can occur.

Kinetic codes take often benefit of spatial symmetry to reduce the number of dimensions. The speed-up is significant - 1D simulation of a typical plasma sheath can take some minutes, 2D simulation several days and a full 3D simulation requires high computing power, usually in a parallelized environment. The 2D kinetic codes are becoming a standard tool on present hardware for probe calibration or plasma sheath modeling, 3D codes are still experimental.

In order to calculate the precise electric force acting on a particle in plasma, it is necessary to take into account interaction between every pair of particles

$$F_i = \sum_{j=1}^n F_{ij} = \frac{q_i}{4\pi\epsilon_0} \sum_{j=1}^n \frac{q_j}{r_{ij}^2}. \quad (2.38)$$

The time dependence of any such algorithm corresponds to $\sim n^2$ in the best case. To improve this dependence, the space region is divided by a grid, the charge density is being calculated on every grid node and then using Poisson equation discrete potential is obtained. This simplification is called *Particle-in-Cell* (PIC). PIC codes have time dependence $\sim n \log n$. The discretization brings the following requirements to ensure correctness of calculations:

- The number of macroparticles in one cell should not be less than 50
- The size of the cell should not exceed the Debye length
- Particle should not cross a whole cell during one time step.

These are very general conditions, which can in fact vary depending on the actual situation. PIC codes are precise when calculating regions, where quasineutrality is not satisfied. In the quasineutral regions (with charge density close to zero) they tend to exhibit numerical fluctuations of electric potential. It is therefore profitable to model quasineutral regions (i.e., the presheath) by fluid codes and the small sheath area by a PIC code.

Despite all listed enhancements, the computational demand of kinetic codes is still an important issue. Much progress has been recently done in discovering new fast methods of solving the Poisson equation (traditionally the most demanding part of the code) and in parallelization of the codes.

2.2.4 Gyro-kinetic modeling

This modeling approach also deals with single particles but uses the guiding-center approach. This allows to increase significantly the time step - in traditional kinetic codes the time step should not exceed the electron gyro-rotation

period. Such enhancement is not very suitable for cases where guiding center motion is not being preserved (i.e., the sheath). However, this approach allows precise simulations of SOL with non-Maxwellian distributions - for example due to heating or current drive. An example of a gyro-kinetic code is Gysela 5D [36], which simulates the whole Tore Supra tokamak in 5 dimensions. A simulation on a supercomputer with 1000 processors is estimated to take about 72 hours, which illustrates the computing demands of these codes.

Chapter 3

Motivation of the thesis

The aim of the thesis is to contribute to ITER related problems by using the PIC modelling. This is motivated by the availability of suitable PIC codes on one side and the existence of ITER issues, which can not be resolved by other means, on the other side. Although the codes were substantially developed in order to calculate desired simulations, the main focus is on the physics, which can be explored by the simulations.

The PIC method can be used to simulate plasma behaviour in the vicinity of solid objects, such as the tiles of plasma facing components or probes. Both of these scenarios are a subject of investigation in this work. The simulations of PFCs concentrate on the gaps between the tiles. These gaps are of interest because of tritium trapped in hydrocarbon layers, which can form inside them. The simulations presented in this work should explain the main mechanisms of plasma penetration into the gaps and provide data for a neutral transport code 3D-GAPS, which models the hydrocarbon layer formation. The aim of the research is to find a geometry of tiles, where the retention is strongly reduced. This would enable the use of carbon in tritium phase of ITER operation.

The gaps are also important in order to estimate the life time of the tiles. The maximum of heat fluxes coming from plasma onto the tiles is usually located near the gap entrance, where the tile surface is almost perpendicular to the plasma flow. The maximum of the heat flux must not exceed the engineering limits of the tiles, or their life time would be significantly reduced. The simulations of the heat fluxes employ for the first time a full 3D3V PIC code SPICE3 and provide corrections to the previous results (obtained by a 2D code). The new effects come from the plasma behaviour in the vicinity of a gap crossing, which could not be modeled in 2D.

The simulations of probes focus on the Katsumata probe, which serves to measure the ion temperature. This is a key parameter needed to calculate

the heat fluxes coming from plasma onto the tiles. The aim of the work is to verify that the probe measures the temperature correctly and explain experimental observations, which are not in agreement with the model of the probe described in literature.

Chapter 4

SPICE2 code

This chapter provides detailed description of the SPICE2 (**S**heath **P**article **I**n **C**ell) code [37][38] used in this thesis. The development of the SPICE code has started in 2004 by Dr. J.P. Gunn (CEA Cadarache, France) and Dr. R. Dejarnac (Institute of Plasma Physics, AS CR). The code was originally one-dimensional with subsequent upgrade to two spatial dimensions. In July 2006 the code was fully functional but its performance was insufficient for realistic simulations. The first step to accelerate the code was done with help of Mgr. Z. Pekarek (KFPP, MFF-UK, Prague) by implementing the fast direct Poisson solver. Further development of the code was then continued in the framework of this thesis.

The brief characterization of the code is:

- 2D in space, 3D in velocity
- Cartesian coordinates
- Dimensionless normalization
- Homogeneous magnetic field with variable inclination towards the surface
- Fast direct Poisson solver
- Injection of particles respecting the orientation of the magnetic field
- Variable geometry with arbitrary number of rectangular, triangular and circular objects
- Parallelization by groups of particles
- Binary output in Matlab format

4.1 Programming environment

The code is written in Fortran 90 and has been successfully compiled by the Intel, PGI and PathScale compilers on both 32 and 64 bit UNIX systems. The output of the code is stored in Matlab v5 binary files, which makes Matlab recommended software for data post-processing. However, the binary format is supported by many other visualization software.

4.2 Normalization

The code uses dimensionless normalization, which scales physical quantities by its typical values. The main advantage of the normalization is the reduction of the number of parameters defining one simulation and so the results of one dimensionless simulation can be de-normalized to a whole set of MKS scenarios. The normalization reads:

$$t \longrightarrow t \cdot \omega_i \quad (4.1)$$

$$x \longrightarrow x/\lambda_D \quad (4.2)$$

$$v \longrightarrow v/c_s \quad (4.3)$$

$$\phi \longrightarrow \phi \frac{kT_e}{e} \quad (4.4)$$

$$m \longrightarrow m/m_i \quad (4.5)$$

$$q \longrightarrow q/q_i \quad (4.6)$$

$$n \longrightarrow n/n_0 \quad (4.7)$$

where ω_i is the ion gyro-frequency, $c_s = \sqrt{kT_e/m_i}$ cold ion sound speed and n_0 the plasma density at sheath entrance. The code is using two important dimensionless parameters:

$$\xi = \frac{r_l}{\lambda_D} \quad (4.8)$$

$$\tau = T_i/T_e \quad (4.9)$$

The parameter ξ is the ratio of the ion Larmor radius and the Debye length, describing the relation between magnetic and electric sheath. The parameter τ is the ratio of the ion and electron temperatures.

4.3 Particle injection

A correct injection of particles is a key point in a realistic plasma simulation. The simplest way of injecting particles from *unperturbed* plasma is to generate their velocities from Maxwellian distributions in all three dimensions. This commonly used technique disregards two important factors: effects of the pre-sheath and presence of the magnetic field.

The SPICE2 code implements more sophisticated approach developed by J.P. Gunn. The distribution function of v_{\parallel} is taken from a quasineutral code *QPIC* [39] (1D code that simulates the whole pre-sheath) or *SOLID* (1D code that simulates the Scrape-off layer). Due to the normalization, the only parameter that affects this distribution is τ , which is kept in most cases close to unity. $f(v_{\perp 1})$ and $f(v_{\perp 2})$ are still Maxwellian. In real plasma such distributions are expected as well as the uniform distribution of the phase of Larmor gyration. This has to be kept in mind when transforming from the B field oriented velocities ($v_{\parallel}, v_{\perp 1}$ and $v_{\perp 2}$) to cartesian velocities. The transformation is as follows

$$v_z = v_{\parallel} b_z + v_{\perp 2} \sqrt{b_x^2 + b_y^2} \quad (4.10)$$

$$v_y = v_{\parallel} b_y + (v_{\perp 1} b_x - v_{\perp 2} b_y b_z) / \sqrt{b_x^2 + b_y^2} \quad (4.11)$$

$$v_x = v_{\parallel} b_x - (v_{\perp 1} b_y + v_{\perp 2} b_x b_z) / \sqrt{b_x^2 + b_y^2}, \quad (4.12)$$

$$(4.13)$$

where b_x , b_y and b_z are directional cosines of the magnetic field

$$b_z = \frac{B_x}{B} \quad (4.14)$$

$$b_y = \frac{B_y}{B} \quad (4.15)$$

$$b_x = \frac{B_z}{B}. \quad (4.16)$$

$$(4.17)$$

This setup generates uniform phase distribution and so avoids density cusps.

When generating the initial particle positions, one has to take into account the orientation of the magnetic field. Assuming zero electric field, particles in homogeneous B field follow a sine curve (in 2D). Apparently, this curve can have many intersections with the injection plane as shown in Fig.

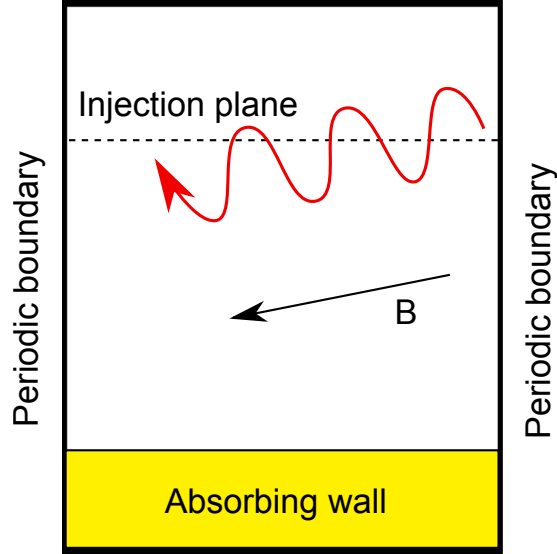


Figure 4.1: Particle injection in SPICE2 code.

4.1. With the standard boundary scenario (when particle leaves the simulation box, it is discarded) one would need to place the particle in the position of its last intersection with the injection plane. This leads to an artificial numerical sheath formation near the injection plane (there are *missing* particles from the previous entrances of particles in the simulation box), which can significantly modify the particle velocity phase-space. The SPICE2 code handles this issue by adding an injection box with length of several ion r_L with zero electric field and injecting particles inside this box. This approach allows proper particle injection, however slows down the calculations (the code has to calculate the movements of particles in the injection box, which do not contribute to the simulation). This problem is a subject of future development. The y position is chosen from a uniform distribution function, the z coordinate from the following formula

$$z = z_{mid} + v_{||} dt R b_z + q v_{\perp 1} m \sqrt{b_x^2 + b_y^2}, \quad (4.18)$$

where R is a random number between 0 and dt , the simulation time step and q and m particle charge and mass. The random term is necessary to avoid artificial modes of the simulation.

4.4 Equation of motion

The SPICE2 code implements standard Leapfrog method [40] for particle advancing. The time step is selected by two empiric criteria: electron should not move through a whole cell during one time step and the time step should be less then 1/10 of electron gyro-period

$$t_{crit_1} = \frac{1}{2} \frac{\sqrt{dz^2+dy^2}}{\xi} \mu \quad (4.19)$$

$$t_{crit_2} = \frac{2\pi}{10\sqrt{\mu}}, \quad (4.20)$$

where μ is the ion-to-electron mass ratio, dz and dy cell dimensions. In most of the simulations $\mu = 200$ is used (instead of real $\mu = 3672$ for deuterium plasma), which allows increasing the time step with a negligible impact on the results of the simulation. In future, the gyro-kinetic method for electrons will be implemented. This will allow further time step increase.

4.5 Weighting

In order to resolve the discretized Poisson equation, it is necessary to build the charge density matrix. The code implements the standard linear weighting scheme Cloud-in-Cell. The charge of each particle is distributed to the four nearest grid points. Using the particle's position, we can split the cell into four regions and use their surfaces to calculate the weights for opposite grid points as shown in Fig. 4.2. This weighting scheme is a compromise between precision and speed of calculation. Zero order weighting (nearest-grid-point) would significantly increase the noise in the charge density matrix and higher order weighting schemes require much more computational time.

4.6 Poisson solver

Solving the Poisson equation and thus obtaining the matrix of the electric field is a fundamental part of every PIC code. In most codes this also represents the part with highest computational demands. SPICE2 implements two different Poisson solvers - the iterative Gauss-Seidel method and direct LU decomposition method [41]. While the iterative solver takes typically 90% of the time step, the direct solver consumes only 5%. This allows parallelization of the code by particle groups. In the following text we will describe more in detail the direct solver developed by Z. Pekarek.

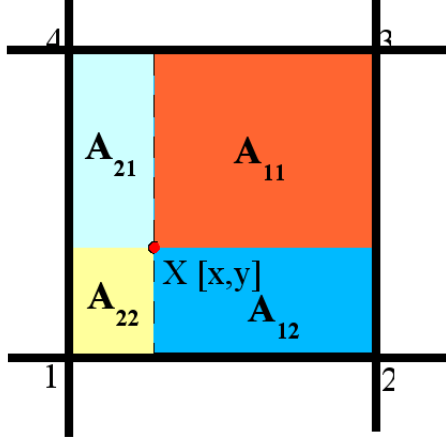


Figure 4.2: Cloud-in-cell first order weighting scheme.

The normalized Poisson equation reads

$$\Delta\phi = -\rho. \quad (4.21)$$

Choosing uniform rectangular grid for discretization of the simulation box

$$y = h_y i \quad (4.22)$$

$$z = h_z j \quad (4.23)$$

The discrete Poisson equation now reads

$$\frac{\phi(i-1, j) - 2\phi(i, j) + \phi(i+1, j)}{h_z} + \frac{\phi(i, j-1) - 2\phi(i, j) + \phi(i, j+1)}{h_y} = -\rho(i, j). \quad (4.24)$$

Potential and charge density matrix are turned into a vector by putting the matrix lines one after another. For this a new index is introduced:

$$k = i + jN_z. \quad (4.25)$$

To keep the explanation illustrative square cells are assumed:

$$h = h_z = h_y. \quad (4.26)$$

We can now rewrite the discrete Poisson equation as:

$$\phi_{k+N} + \phi_{k+1} - 4\phi_k + \phi_{k-1} + \phi_{k-N} = -\rho_k h^2 \quad (4.27)$$

The Laplace operator in Poisson equation is transformed into a matrix. This matrix will have $m \times m$ cells, where m is $N_z \times N_y$. This means that the size of the matrix will grow as N^4 , while most of the members will be zero. To avoid immense memory requirements, the *sparse matrix* format is used. This is achieved using the UMFPACK library [42]. To solve the Poisson equation, Laplace matrix is inverted (once at the beginning of the simulation) and then every time multiplied with the vector of the charge density in order to obtain the potential

$$\phi = -\Delta^{-1}\rho. \quad (4.28)$$

This approach has a number of advantages. In general it is much faster than the iterative solvers and the calculation of the potential has constant computational demands. Limitations of the method come at the first step, there has to be enough memory for the matrix inversion. The inversion itself is done by the LU decomposition by the GotoBLAS [43] library. A matrix of the grid 6000x2000 cells has been successfully inverted, which is far beyond the usual grid size (500x400).

4.7 Boundary Conditions

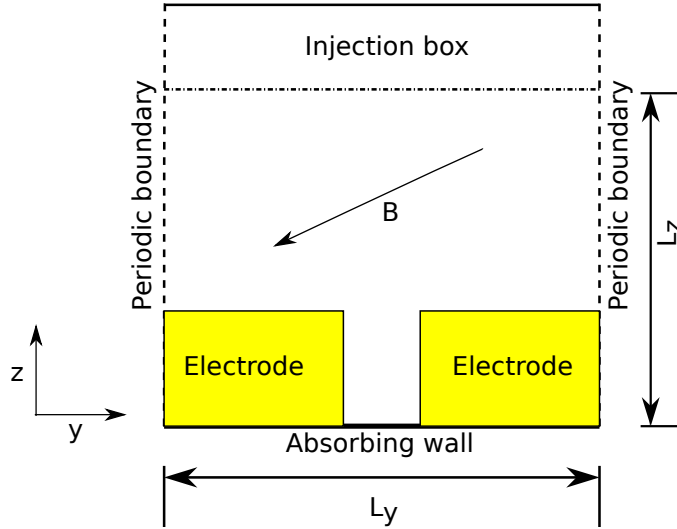


Figure 4.3: Geometry of the SPICE2 simulation.

Figure 4.3 shows schematically the boundaries in present code geometry. The top boundary, which corresponds to the injection plane, is fixed, we impose zero potential (unperturbed plasma). There is the injection box above

the top boundary, so particles are being discarded only if they reach the top boundary of the injection box. Side boundaries are periodic, particles crossing them are being shifted by L_y or $-L_y$, respectively. The bottom boundary is again fixed, with the same imposed potential as the potential of the tiles, particles are being discarded when they reach it (simulating perfectly absorbing surfaces). The tiles are equipotential boundaries. The coordinate system is cartesian, with y direction parallel to the injection plane and z direction parallel to the gap.

4.8 Parallelization

4.8.1 Particle decomposition

The SPICE2 code is parallelized using the OpenMPI library [44]. In theory it allows to run on 99 parallel threads, however various scaling constrains limited this number to some 4 - 8 threads. The original parallelization was done by particle decomposition (each processor has a certain number of particles) unlike the usual domain decomposition (each processor takes care of a part of the simulation box). This parallelization was possible only due to the fast Poisson solver. All remaining parts of the code could be calculated separately. This approach minimized the network traffic, which would otherwise be linked to particles crossing domain borders. The workflow of the code is schematically described in picture 4.4. The only traffic related to the parallelization is the transfer of charge densities calculated by each thread and then the distribution of the actual potential.

4.8.2 Domain decomposition

While the particle decomposition was suitable for simulations on 2 or 4 core processor machines, some simulations required much more computing power, which was only available at the High Power Computing centers (HPCs), such as HPC-FF at Forschungszentrum Juelich. The HPCs have typically ~ 1000 cores, however, the computation time is strictly limited to approximately 1 day. This setup favors massively parallel codes, which can benefit out of the large number of cores. In order to adapt the SPICE2 code for the HPC environment, a new parallelization scheme had to be implemented. The problem of particle decomposition is that some parts of the code did not scale with the number of particles involved but with the size of the grid. This remains constant as each processor works with the entire simulation box.

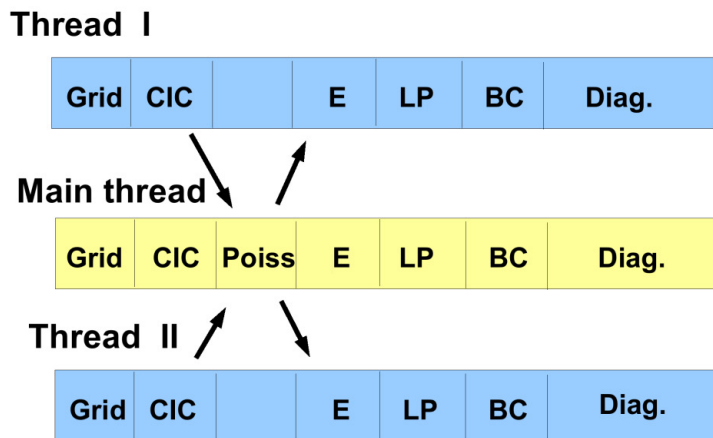


Figure 4.4: Workflow of the SPICE2 code.

The parallelization scheme has been therefore changed to domain decomposition, so that each processor now takes care of a spatial slice of the simulated box specified by limits z_{start} , z_{stop} , y_{start} and y_{stop} . The number of slices in z and y direction are specified in the input file (optional *domaindecomp* namelist), the sizes of the slices are fixed and distributed equally. The poisson solver is still not parallelized, calculated by the first processor.

The new scheme required a number of changes in the code. The subroutines which were handling 2D spatial matrices (i.e., the charge density matrix) are now modified to take care only of a part of these matrices, according to their spatial limits. In addition a new parallelization routine had to be added, which handles particle transfers between the slices. The standing implementation first runs across the particle vectors and checks whether they do not lie outside the given spatial limits. If this is the case, then it moves them to one of the available 8 buffers. Then it exchanges particles with the 8 neighbor-hooding slices. This is rather demanding on available memory, since each of the 8 buffers has to be large enough to hold all the particles of a given slice.

The properties of the new decomposition scheme is demonstrated in Fig. 4.5. The studied case was a 100x1000 grid without internal electrodes with domain decomposition $2 \times M$ slices, where $M = N/2$ (N is the number of processors). Solid red line shows the scaling for the new scheme. The scaling is better than with the old scheme (blue line), however, limited by the ineffective division of the simulated box. The transition from a single processor run (= the processor takes care of the entire simulation box) to 2 processor

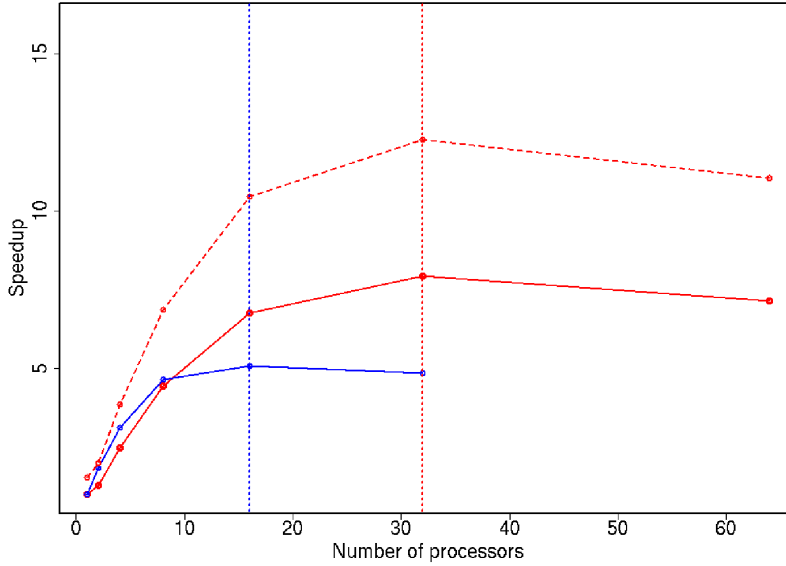


Figure 4.5: Scaling comparison between old (blue) and new (red) parallelization scheme. The red dashed line shows speedup of the new scaling without the decomposition penalty.

parallel run implies division of the box in z direction. All the other transitions to higher number of processors involve division in the y direction (to keep $2 \times M$ decomposition). The profiles of particle densities are constant in the y direction but vary in the z direction, which means that when we divide the box in z direction, each processor may take care of different number of particles. This problem is visible in Fig. 1, the speedup between 1 and 2 processors is only 1.3x, while between 2 and 4 processors it is 1.93x. This issue can be solved by iterative optimization of the division in the z direction. To estimate the scaling which would not be affected by the decomposition penalty, the speedup can be calculated based on the time of the 2 processor run. This line is shown as a dashed red line, which peaks at speedup 12x at 32 processors. Moreover the optimization of the code brought speedup 1.36x of the single processor runs.

The effectiveness of the domain decomposition is limited by the ratio of cells contained in one slice to the number of border cells between the slices. The exact limit is still to be determined, however it is not advised to use slices smaller than 30 cells in any direction. If this limit is not reached, the new scheme proved to be effective up to 32 processors (the previous scheme had a limit at 8 processors). Further parallelization is limited by the poisson

solver, which is not parallelized.

For the purpose of this thesis, the standing implementation of the domain decomposition is sufficient to achieve required simulations. The duration of simulations did not exceed 1 month in any case. Future development will target optimization of the parallelization in order to enable simulations of more demanding scenarios.

4.9 I/O files

The SPICE2 code uses concept of the input file, which allows to run multiple simulations without compiling the code for each scenario. The input file is a simple text file and it allows to set all simulation parameters. For precise documentation of the input file format, see the code documentation [45].

The code produces three types of output files, all of them in Matlab v5 format. One output file (specified with the `-t` flag) stores all optional diagnostics, time histories, actual charge density and potential. This file is being produced every k steps (defined in the input file). Another file (defined by the `-o` flag) stores time-averaged diagnostics from the steady state regime. It is being saved every N steps once the simulation reaches the steady state. The last set of files stores the positions and velocities of particles. Such file is produced for every processor. This method is designed to minimize network traffic - files with particle positions are typically memory-consuming and rarely needed. The separation of time histories from time-averaged diagnostics simplifies post-processing. The code allows two ways of relaunching a simulation. First is so-called *continue* mode, where the code resumes particle positions, time histories and time-averaged diagnostics. It is designed for incidents when the simulation was aborted. Second is *restore* mode, where the particle positions are restored and time is set to the beginning of steady state. This mode allows modification of the input file (i.e., different diagnostics).

Chapter 5

Simulations of the TEXTOR tiles

5.1 Introduction

This chapter presents results of simulations of plasma interaction with the TEXTOR test limiter. The motivation of the research related to carbon deposition inside the gaps has been explained in chapter 1.4.1. Here we recall that there are two objectives of these simulations - to understand the mechanisms of plasma interaction with the complex gap geometry and to provide flux profiles for the neutral transport code 3D-GAPS, which can simulate the hydrocarbon layer formation. The content of this chapter was used in a manuscript, which has been submitted to *Plasma Physics and Controlled Fusion*.

5.2 SPICE2 setup

The general geometry of SPICE2 gap simulations consists of an injection plane (top boundary in Fig. 5.1) with imposed value of plasma potential $V_{pl} = 0kT_e$, two periodic side boundaries and a bottom absorbing equipotential wall at floating potential $V_{fl} = -3kT_e$. In the simulated region, there are two electrodes representing the tiles. Experiments with the TEXTOR test limiter have been done with unshaped (Fig. 5.1A) and shaped (Fig. 5.1B) gaps to investigate the impact of shaping on the plasma deposition inside the gaps. The gaps used in the experiments are 0.5 mm wide and the tiles are 10 mm long. The magnetic field is inclined at 20 degrees with respect to the flat top surface of the unshaped gap. In the case of shaped gaps, the top surfaces are inclined such that one is parallel to the magnetic field and the

other one has an inclination of 40 degrees with respect to the field lines. In the described experiment, all the gaps were more than 10mm deep, however only the first 2 mm were simulated, as the plasma does not penetrate any deeper.

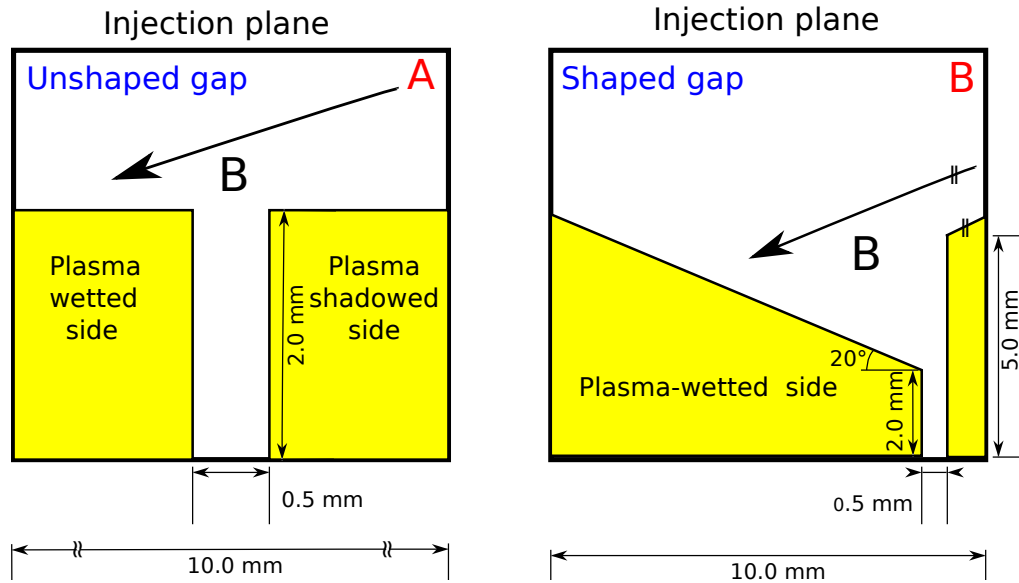


Figure 5.1: Geometry of the gaps. A - unshaped gaps, B - shaping used in TEXTOR test limiter.

5.3 Results of simulations

5.3.1 Unshaped gaps

Standard case

First, let us study the effect of this gap geometry on the plasma deposition profiles for fixed plasma conditions. We define the *standard* case with typical conditions of the TEXTOR SOL as follows:

- Plasma density $n = 6 \times 10^{18} \text{ m}^{-3}$
- Electron temperature $T_e = 30 \text{ eV}$
- Deuterium ion temperature $T_i = 60 \text{ eV}$
- Magnetic field magnitude $B = 2.25 \text{ T}$

- Magnetic field inclination $\alpha = 20$ degrees with respect to the top surface of an unshaped gap

The main mechanism governing plasma behaviour in the vicinity of the gaps is the gyro-motion of particles. Ions have Larmor radii comparable to the size of the gap ($r_{L_i} = 0.35$ mm) enabling them to penetrate into the shadowed region. Electrons are strongly magnetized and simply follow the field lines, as there is no mechanism of cross-field transport implemented in the model. This Larmor effect results in net positive space charge inside the gap and subsequent formation of a potential peak (as seen in Fig. 5.2). Incoming deuterium ions can be divided into three categories - some hit the plasma wetted side of the gap (Γ_a), others fall onto the shadowed gap side (Γ_b) and the rest is deflected from the gap and hit the top surface of the tiles (Γ_c) [46].

The profiles of D^+ fluxes along the gap sides are shown on Fig. 5.3 (black lines). The left side of the gap, which is open to direct plasma flux Γ_a , shows a complex decay structure. Near the entrance, there is a plateau region followed by an exponential decay. The transition occurs at the projection of the lowest magnetic field line which is not intercepted by the right tile. The plateau is formed due to ions which are prevented from flowing deeper in the gap by the potential peak. We also observe an ion flux Γ_b falling on the right side of the gap, although it is in the plasma shadow. The total amount of flux is approximately one order of magnitude lower than the plasma wetted side. The distribution of particle fluxes shows that typically 5% of particles reach the right side of the gap, 75% the left side of the gap and the remaining 20% are prevented from entering the gap and hit the top surface.

In order to explain the mechanism which can lead to particle flux Γ_b falling onto the shadowed side of the gap, we have followed the magnetic field line which passes close to the corner of the right tile (see Fig. 5.4 left). The total electric field felt by an imaginary sensor which would follow this field line, divides the trajectory into three sections as we can see in Fig. 5.4 (right), plotted as a function of parallel coordinate l . Far from the gap ($l > 150$) the total electric field is positive and first acts towards the tiles (there is a regular sheath potential drop). Once the sensor enters the gap ($125 < l < 150$), the electric field changes sign and points in the direction of the plasma shadowed side. Finally, when the sensor approaches the plasma wetted side of gap ($l < 125$), it changes sign again and acts towards the surface. The arrows representing the direction and magnitude of the local electrical field show that there is indeed a region inside the gap, where the field attracts ions towards the plasma shadowed side of the gap. Since the ion Larmor radius is comparable to the gap size and so much larger than the typical scale of variation of the local strong electric field, the ions behave as

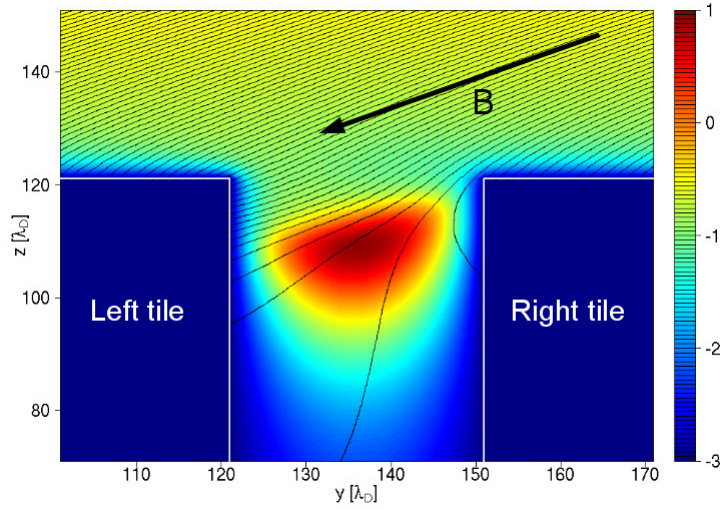


Figure 5.2: Potential profile of the standard case. Black lines represent deuterium ion streamlines. Potential in kT_e , dimensions in Debye lengths. In absolute units the gap is 0.5 mm wide.

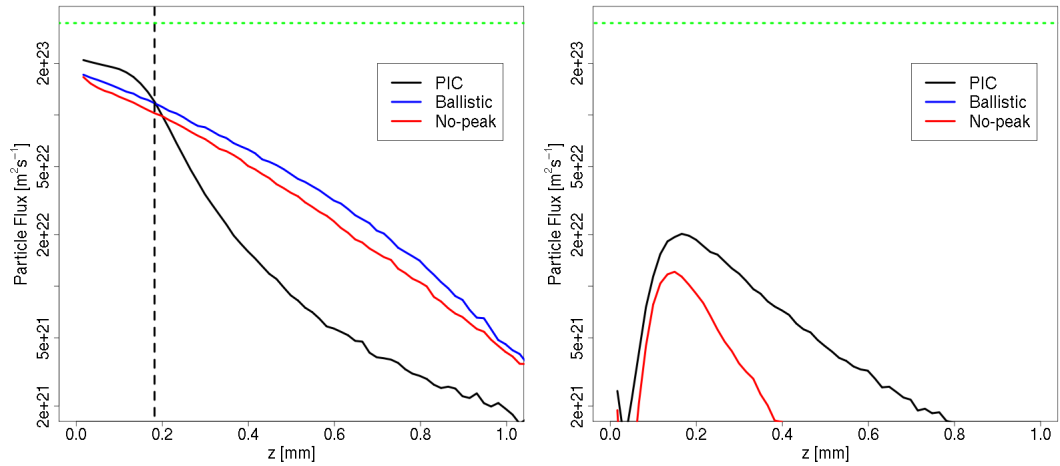


Figure 5.3: Deuterium fluxes along the gap on the plasma wetted side (left) and plasma shadowed side (right). Black curves represent the regular PIC simulation, red curves simulation without the potential peak and blue curves the ballistic case. Gap entrance corresponds to $z = 0$ m. Black dashed line shows the geometrical projection of plasma wetted area, the green dotted line shows projection of incoming particle flux on the gap side.

demagnetized inside the gap.

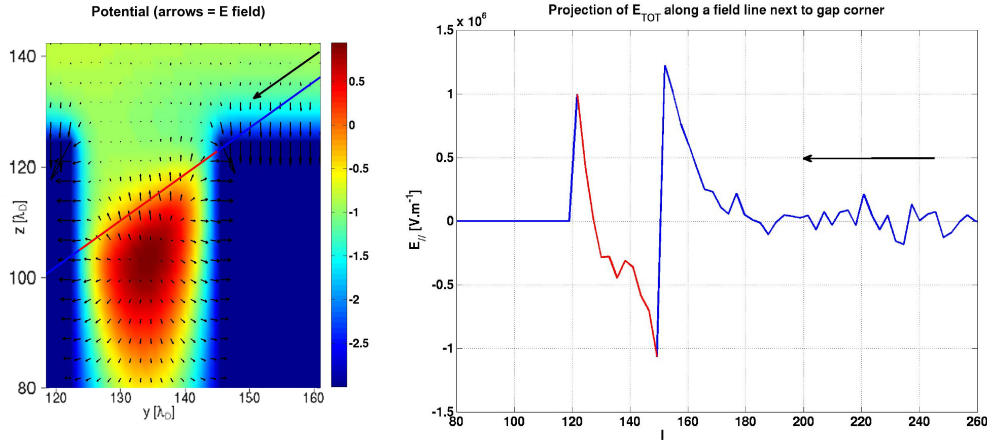


Figure 5.4: Detail of electrical potential in the vicinity of the gap (left) with local electric field (arrows) and the projection of the total electric field on a B field line passing next to the tile corner (right).

In order to investigate the influence of the potential peak and sheath electric fields on the plasma penetration into the gap, the PIC simulation has been compared with two special non-selfconsistent cases with fixed imposed potential. One is the ballistic case (with zero electric field), second is a case with potential similar to the steady-state result of the PIC simulation but the potential peak has been manually erased. The latter will be called *no-peak* further in the text. Fig. 5.3 shows comparison of the three cases. It is visible that ions penetrate deeper in the gap in the no-peak case compared to the self-consistent PIC simulation. This demonstrates that the potential peak acts as a barrier that regulates the ion flux according to its magnitude. It is also partially responsible for the ion flux, which is pushed towards the plasma shadowed side. In both cases, the total fraction of ions deposited inside the gap is $\sim 80\%$, which means that the fraction of deflected particle remains almost unchanged ($\sim 20\%$).

In the ballistic case, there are no particles hitting the plasma shadowed side and the particle flux on the plasma wetted side is increased compared to the PIC run. The fraction of deflected particles is below 5%, which is the precision level of the diagnostics for flux recording. It can be seen that the fluxes in all three cases are lower than the unperturbed flux coming from plasma and falling onto a surface with the same orientation as the gap (dotted green line).

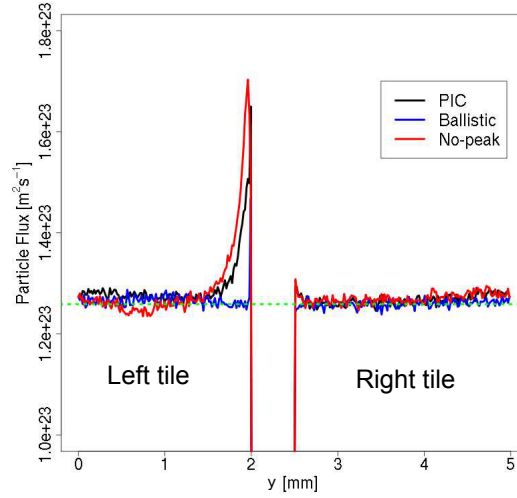


Figure 5.5: Deuterium fluxes falling onto the top tile surface. Black curves represent the regular PIC simulation, red curves simulation without the potential peak and blue curves the ballistic case. Green dotted line shows the projection of particle flux onto the top surface.

Particles Γ_c , which are deflected from the gap, reach the top surface of the next tile, where a peak of particle flux is observed in the vicinity of the tile corner (see Fig. 5.5). The corner peak is present for PIC and no-peak case, which indicates that is not caused by the presence of potential barrier at gap entrance. It is not present in the ballistic case, which confirms that the particles are deflected by the electric fields associated to sheath potential drop at the top tile surfaces.

These results lead to a conclusion that while the electric fields associated with the sheath in this complex geometry affect the fraction of particles which are prevented from entering the gap, the potential peak is responsible for the distribution of ion fluxes inside the gap. The combination of both mechanisms is responsible for the flux falling on the plasma shadowed side.

Parameter study

A set of simulations with varying plasma parameters was performed in order to investigate the effect of different plasma conditions on the deposition profiles for the fixed geometry. The plasma density was varied over the range 2×10^{18} and $1 \times 10^{19} \text{ m}^{-3}$ and the electron temperature between 20 and 50 eV, which are characteristic for TEXTOR SOL. The magnitude and orienta-

tion of the magnetic field and ratio of temperatures was kept constant, same as in the standard case. As shown in the standard case, the crucial element governing the particle fluxes along the gap is the potential peak near the entrance of the gap. The maximum value of the electric potential in the positive space charge region for all the studied cases is summarized in Fig. 5.6. A white dashed line, where the peak height is equal to the plasma potential, separates zones with different influence of the potential peak as it will be explained further in this section.

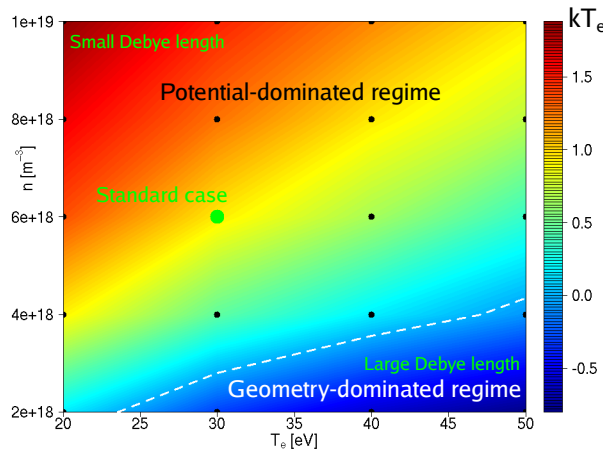


Figure 5.6: Maximum of potential at the potential peak inside the gap. Contour lines separate the zones of strong and weak influence of the peak.

The simulations reveal that the magnitude depends on the Debye length and for gap width comparable to the ion Larmor radius can be fitted by the following function:

$$\phi_{max} \sim -e\sqrt{\lambda_D} \quad (5.1)$$

as shown in Fig. 5.7. This is in a contrary with an intuitive expectation, which would favor ion Larmor radius as the key parameter determining the ion penetration inside the gap and subsequent space charge formation. It is the consequence of the demagnetization of ions in the strong electric field localized near tile surfaces.

Fitting of the particle fluxes

In order to facilitate implementation of the particle fluxes into the 3D-GAPS code, the flux curves had to be represented by analytical functions. For

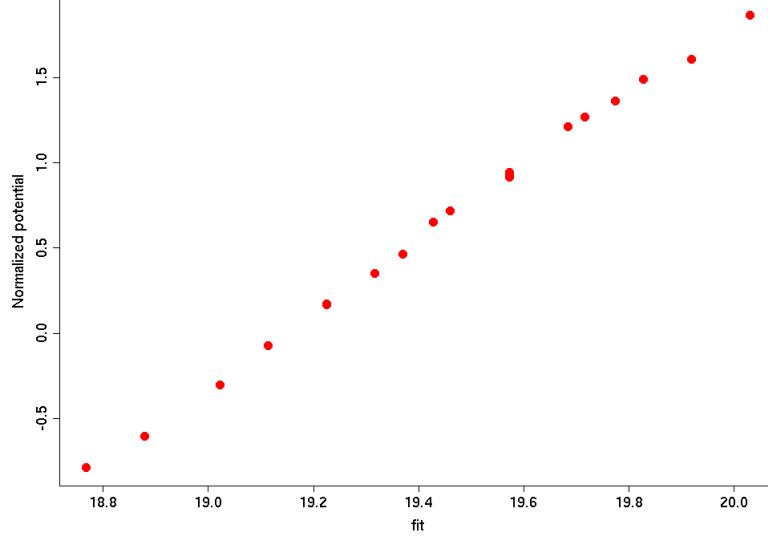


Figure 5.7: Height of the potential structure modeled by function 5.1.

this purpose, a fully automatic fitting procedure was developed. The flux curve is split into 2 regions - the decay deep inside the gap (modeled by an exponential) and the main flux, which is fitted by a parabola. This fitting scheme proved to be quite robust and was capable of approximating the fluxes for all studied cases and for both tiles within the precision of 10%. An example of such fit is shown in Fig. 5.8.

Debye length study

To demonstrate the differences in plasma behaviour, we have selected two extreme cases - small Debye length $\lambda_D = 1.05 \times 10^{-5}m$ ($n = 1 \times 10^{19} \text{ m}^{-3}$, $T_e = 20 \text{ eV}$) and large Debye length $\lambda_D = 3.71 \times 10^{-5}m$ ($n = 2 \times 10^{18} \text{ m}^{-3}$, $T_e = 50 \text{ eV}$). Direct comparison of the flux profiles (Fig. 5.9) shows that the deposition of plasma inside the gap can be in two different regimes. In case of small Debye length (Fig. 5.9A), the potential peak is well developed (maximum of potential $1.4 kT_e$ above the plasma potential as shown in Fig. 5.6) and the transport barrier inside the gap gives rise to a plateau region near the gap entrance (this region is directly wetted by plasma) and then decays exponentially. In case of large Debye length (Fig. 5.9B), there is almost no visible peak and so the decays are exponential. The transition between the 2 regimes is smooth. Dashed lines in Fig. 5.9 show the particle flux profiles for

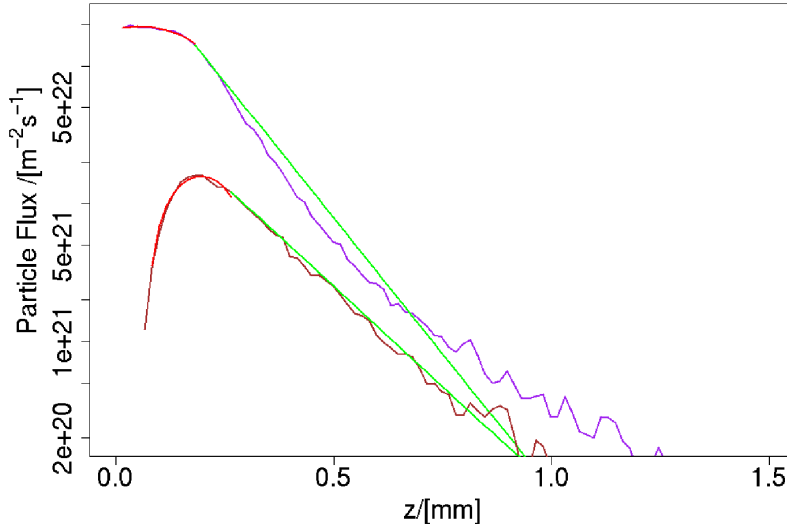


Figure 5.8: Fitting of the particle fluxes inside the gap for the standard case. Red curves are parabolic fits, green curves exponential fits.

the ballistic simulation. Similarly to the results of the standard case, there is no particle flux observed on the plasma shadowed side.

In order to quantify the plasma penetration inside the gap, we define the *decay length* L_d as the distance from the gap entrance, where Γ_a falls below 1/1000 of the maximum flux. In the case of small Debye length $L_d = 0.77$ mm, while in the case of Large Debye length it doubles to 1.76 mm. This is the main difference of the two regimes - the barrier formed in the potential dominated regime prevents ions from entering deep inside the gap.

The distribution of fluxes on gap sides shows little variation with changing plasma conditions. On average, 70% of the incoming flux falls on the plasma wetted side of the gap, 5% hits the plasma shadowed side and 25% is deflected and reaches the top surface of the tile. These extreme cases were compared to ballistic simulations and in both cases the fraction of deflected particles dropped to 5%, which verifies the role of sheath electric fields.

5.3.2 Shaped gaps

The purpose of tile shaping is to mitigate unfavourable transport into the gaps and protect the tile edges from extreme heat loads. Since it is unclear where to define entrance of the gap (see Fig. 5.10), we have decided to

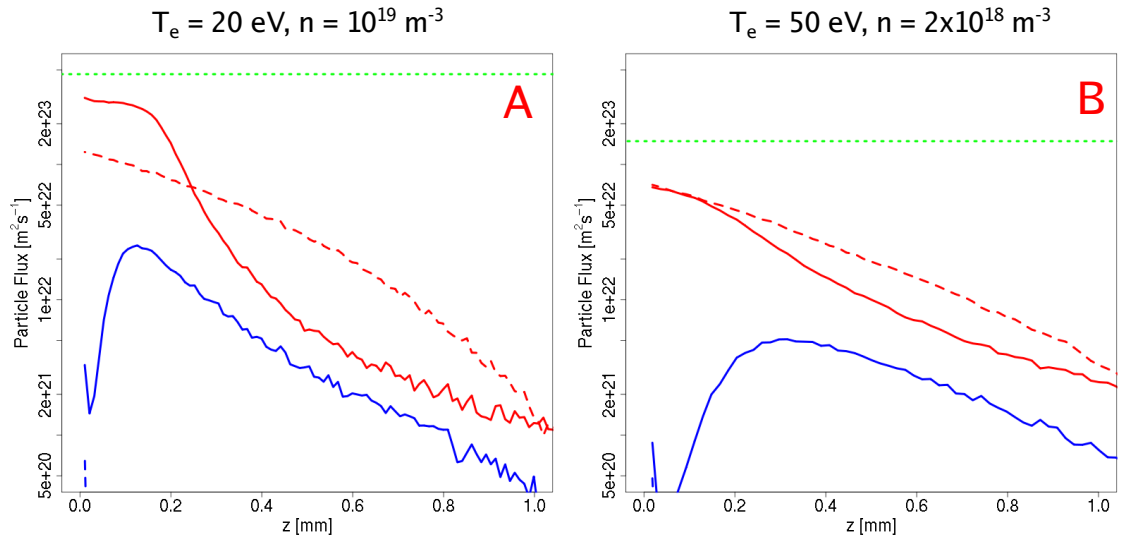


Figure 5.9: Deuterium ion flux profiles inside the gap for the extreme cases. A - small Debye length, B - large Debye length. Plasma wetted side in red, plasma shadowed side blue. Dashed lines show the ballistic case. Green dotted lines show the projection of parallel particle flux.

define the gap where the 2 tile sides are parallel ($z < 2$ mm). The remaining part of the right tile which faces inclined top surface of the left tile ($2 \text{ mm} < z < 5$ mm) is called *Shadowed part of the right tile*. A simulation for the standard conditions as used in case of an unshaped gap reveals that due to the large shadowed region, the potential peak is well developed and can rise $3kT_e$ above the plasma potential. This determines the transport regime in the vicinity of the gap. The flux on the right tile side is shown in Fig. 5.11 (right). It is seen that the flux on the shadowed part of the right tile drops quickly and there is no flux inside the gap. This behaviour has been observed for all cases with varying plasma conditions (in the same range as in case of unshaped gaps). This is an important demonstration of the effectiveness of tile shaping. The flux on the top left inclined surface (Fig. 5.11 left) is almost constant on the plasma wetted part of the tile ($y \lesssim 5$ mm) and decays inside the shadowed region (separated by the black dashed line). Comparison with the ballistic case (blue lines) confirms that the potential peak works as a barrier for ions.

In order to estimate the influence of the shaping on the plasma deposition inside the gap, the shaping parameter H (see Fig. 5.12) was varied from 3 mm (strong shaping) to 0.2 mm (weak shaping) for the standard plasma

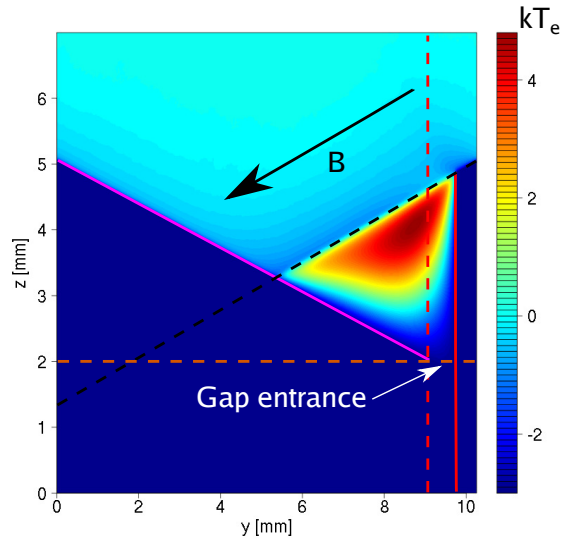


Figure 5.10: Potential distribution in the shaped gap for standard conditions. Magenta and red lines correspond to fluxes shown in Fig 5.11

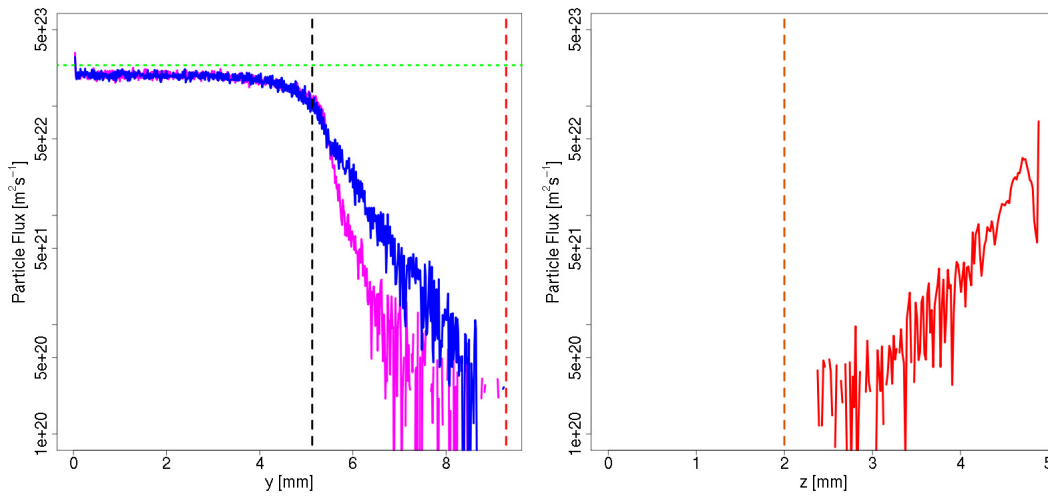


Figure 5.11: Particle fluxes along top left tile surface (magenta) and the right tile (red) in the shaped gap for standard conditions. The particle flux along the left tile inside the gap was negligible and as such not shown. Blue line shows the result of a ballistic case.

conditions as defined in section 5.3.1. This had a direct effect on the inclination of the tile top surface with respect to the magnetic field, which changed from 40 to 21.3 degrees. The shaping was changed so that sum of L and H was constant, equal to 5 mm. The simulations show that the magnitude of the potential peak was decreasing with decreasing shaping but even for the weakest shaping the gap was still in potential dominated regime (potential peak maximum equals to 0.74 kT_e). The effect on the plasma fluxes is demonstrated in Fig. 5.13, where we have plotted the deposition profiles on both sides for varying shaping. The potential peak is effective in protecting the plasma wetted side of the gap but at the same time it pushes a fraction of the incident ions to the plasma shadowed side. For weak shaping (which is more ITER relevant), the ion flux profile on the plasma wetted side already resembles to the unshaped case, with a typical plateau region near the gap entrance.

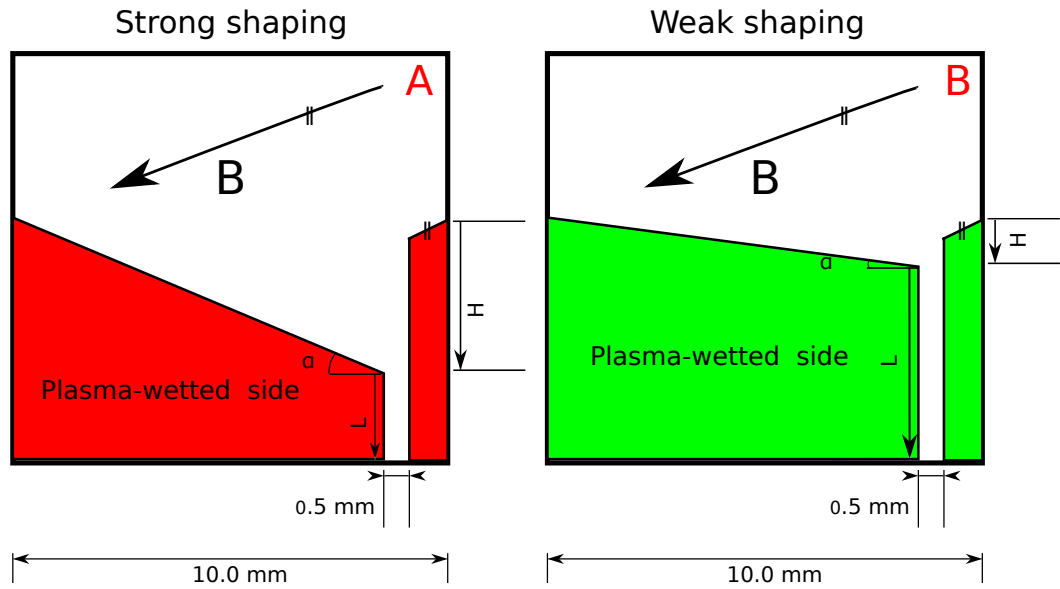


Figure 5.12: Geometry of the tiles with strong (left) and weak (right) shaping. The shaping parameter H is varied, which affects angle α of the top tile surface.

5.4 Summary of the TEXTOR simulations

The plasma behaviour in the vicinity of TEXTOR tiles with shaped and unshaped gaps was simulated using the 2D3V particle-in-cell code SPICE2.

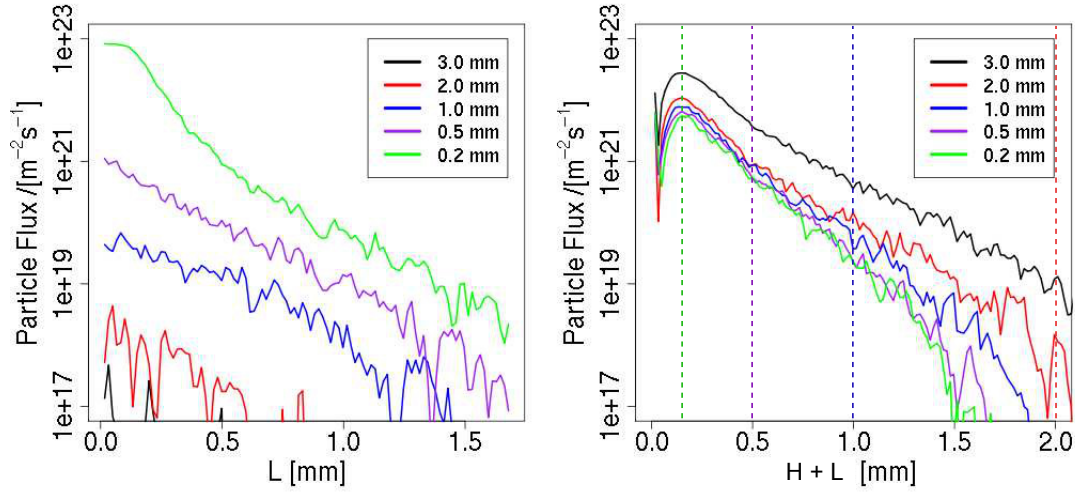


Figure 5.13: Deuterium flux profiles along the plasma wetted side of the gap (left) and plasma shadowed side (right) for different shaping (3.0, 2.0, 1.0, 0.5 and 0.2 mm).

The sheath electric fields near to tile surfaces are responsible for the amount of particles which enter the gap, while potential peak formed near the gap entrance was identified as the main factor influencing the plasma deposition inside the gap. Depending on the plasma conditions the ion flux profiles along the gaps are mainly influenced by the potential peak (potential dominated regime), with high flux region located near the gap entrance and fast decay for the plasma facing side of the gap, or by the geometry of the gap (geometry dominated regime) with slow exponential decay of the flux. The transition between the regimes is smooth and can be observed when the maximum of potential peak exceeds the plasma potential and so that it can effectively block ions from entering deep inside the gap. This maximum was found to be dependent on the Debye length. The main consequence of the two regimes is the influence on decay length L_d , which is twice longer (1.76 mm) for geometry dominated regime than for the potential dominated regime (0.77 mm) for unshaped gaps. In case of shaped gaps, all studied cases were in the potential dominated regime. The study of shaped gaps has shown that in case of strong shaping there is a large potential peak which can protect the gap from incoming ion flux, however such geometry would result in elevated heat fluxes on the top tile surface (the magnetic field has inclination of 40 degrees with respect to the top surface of the tile). There is also a significant

ion flux deflected by the potential peak onto the plasma shadowed side of the gap. In case of weak shaping the flux profiles indicate a transition to the unshaped gap. The fluxes obtained from the simulations were used as input for the 3D-GAPS code [47] to study hydrocarbon layer formation inside the gaps.

Future studies will involve simulations of more ITER relevant geometries with magnetic field at oblique angle with respect to the top tile surface. Such simulations should verify the applicability of tile shaping for the ITER divertor.

Chapter 6

Simulations of the Katsumata probe

6.1 SPICE3 - description

The SPICE3 code has been developed as an extension of the existing SPICE2 code. It is a 3D3V Cartesian code, with most of the routines identical to SPICE2 code as described in chapter 4, just the x direction has the same role as y direction, i.e., all side boundaries are now periodical. The development of SPICE3 has been motivated by the existence of scenarios, which could not be reduced to two spatial dimensions. Two examples of such scenarios are studied in the following two chapters.

6.1.1 Poisson solver

The new routine in SPICE3 is the Poisson solver (developed by Z. Pekarek), which is now based on multigrid method. The PIC method requires several features from the numerical method used to solve the Poisson equation, sorted here by their importance:

- the solver should handle effectively both the desired shape of cells (usually a square/rectangle) and the solid surfaces which might be curved and/or not aligned to the grid,
- due to the iterative nature of the PIC method the solver should utilize the similarity of consecutive steps,
- the choice of boundary conditions provided by the solver should reflect both the plasma/solid setup being studied and the limits of the PIC model stability,

- since the PIC method uses derivatives of the potential, the required precision in case of an iterative solver depends on the solution smoothness and distribution of residual error (these might be different across methods such as Jacobi, SOR or conjugated gradients),
- for modelling of rf or floating potential setups the ability to easily update the potential of an electrode can significantly speed up the computation,
- it would be desirable to model the change of shape of the solid surface due to e.g. erosion and deposition or electrode movement without the loss of similarity in consecutive steps.

We have met these specifications with a numerical method based on the multigrid approach [48, 41], augmented with a direct solver based on LU decomposition [41, 42] of the discretized Poisson equation [41].

The multigrid principle is based on an observation of residual error, defined as $d = Lu_{\text{est}} - f$ the difference between the current estimated solution and the input charge density, and the handling of this difference in basic iterative methods during their convergence to the precise solution. Given a characteristic size of the cell, the high frequency components of the residual get smoothed in several iterations, while low frequency, or almost constant, components are with traditional iterative methods smoothed relatively slowly.

Since the discretization of the setup through a PIC grid is an artificial construct, we can build another grid (usually twice coarser in each dimension) or a series of grids, a *multigrid*, to efficiently destroy the relevant component frequency of the residual error through smoothing on the appropriate coarser level.

Obviously for PIC applications the grid is finite, which limits the number of grids necessary; the layout and geometry of solid surfaces included in the setup can further limit the amount of multigrid levels. The residual error from the finest grid level is transformed (via the *restriction* operator) onto the coarsest grid, where the direct solver transforms it into a *solution update* which negates the error. This update is then gradually projected (via the *prolongation* operator) onto the finest, input grid while also on each grid level being *smoothed* usually by the Jacobi or Gauss-Seidel method.

This process is then repeated until the residual error diminishes sufficiently, as with any iterative method.

A method constructed this way then meets the desired properties set by the PIC application:

- grid structure is preserved on the finest and coarser levels, electrode configuration is transformed with resolution better than the cell size,
- the LU decomposition based direct solver and other data structures are constructed only once for each electrode layout,
- the implementation currently supports both fixed and periodic boundary conditions, with no obvious limits on other types of boundary conditions,
- the method of computing residual error, the stopping criterion and the smoothing subroutine are identical to the Gauss-Seidel or Jacobi method,
- setting a new value of potential on a fixed node of the grid does not trigger any costly subsequent recomputation of internal data structures,
- the change of grid node status from fixed potential to Poisson equation driven, and vice versa, does not always trigger recomputation, although the performance might slightly diminish.

The method has been tested and benchmarked against analytical solutions, Jacobi and Gauss-Seidel method and the direct solver based on LU decomposition. While the performance is better than the iterative methods and worse than the direct solver, in 3D the prohibitive memory consumption of the direct solver makes the multigrid method the preferable option with its modularity enabling optimal balance of performance and memory consumption.

6.1.2 Simulation limits

The calculations are restricted by the size of the PIC grid, the current limit is 128x128x128 cells on available computers. The size of the cell has to be equal or smaller than the Debye length in order to avoid numerical instabilities. This creates a window of plasma density/temperature combinations, which can be simulated on accessible hardware. The code can simulate plasma with a range of T_i/T_e ratios between 0.1 and 10, typical for the tokamak SOL conditions. The magnetic field strength, which can be simulated, is restricted by the necessity to resolve the magnetic pre-sheath within the simulation box, which extends several ion Larmor radii into the plasma. This makes strong magnetic fields (smaller ion Larmor radius) easier to simulate, an advantage for studies of tokamak plasma.

6.2 Simulations of the Katsumata Probe

As described in the first chapter, measurements of the ion temperature SOL are essential in order to calculate the power fluxes falling onto the divertor tiles. Modeling of probes in general is one of the domains, where the PIC simulations apply. The dimension of probes are typically on the same scale as ion Larmor radius and as such the finite Larmor effects cannot be neglected. The Katsumata probe as described later lacks symmetry and as such its model cannot be reduced to less spatial dimensions. Full 3D3V simulations are therefore necessary. The main aim of this chapter is to explain the plasma behaviour in the vicinity of such a probe and to verify the experimental technique used to determine T_i . The content of this chapter is substantially based on a published article [49].

The Katsumata probe shields its collector from electron current in order to achieve sensitivity to the ions. According to the basic theory [50], the shielding is provided by the geometry of the probe and its orientation with respect to the magnetic field. A scheme of this principle is shown in Fig. 6.1. A cylindrical collector is submerged into a metal tube, with axis perpendicular to the magnetic field. Ions with Larmor radii comparable to the probe size can penetrate into the tube and reach the collector, while electrons should be screened. The ion temperature is obtained from the fit of the I-V characteristics [33]. A variant of the probe, which serves for measurements of the plasma potential, the ball-pen probe [51], has been recently developed and used on a number of tokamaks [52] [53].

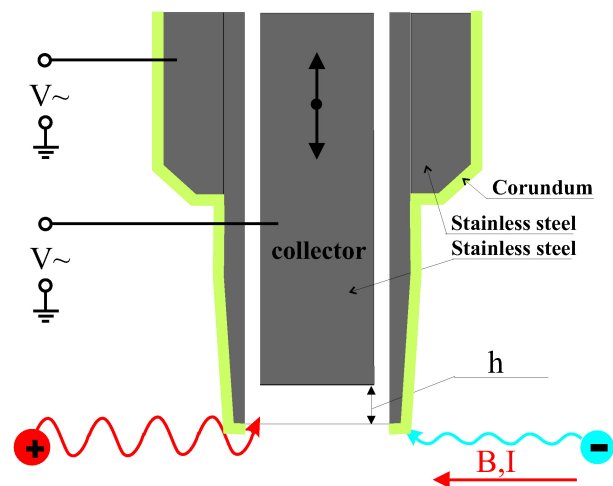


Figure 6.1: Schematics of a Katsumata probe.

This simple geometrical model has been contradicted by experiment [33], where the electron shielding was only efficient for the case when the tube was biased on the same potential as the collector.

6.2.1 Geometry of the probe model

The setup of the simulations is shown in Fig. 6.2. The simulation region is of cubic shape, with the probe in the lower part. The probe consists of 3 conductors - the top surface, which is left at floating potential V_{fl} , the tube with variable potential V_T and the cylindrical collector pointed in direction of the z axis with potential V_C . The plasma potential is defined at the top boundary of the simulation region and is equal to zero. The particles are injected from the top boundary and follow the magnetic field lines, which are inclined at oblique angle with respect to the top surface. This is a difference between the simulation model and the experimental setup, which is required by the SPICE3 code in order to speed up the calculations. The validity of the model is discussed in section 6.4.1. The side boundaries are periodical. The collector is submerged inside the tube by a variable distance h (distance between the top surface and collector ending). The inner diameter of the tube is 2 mm, while the collector's diameter is 1 mm. The depth of the tube is 2 mm.

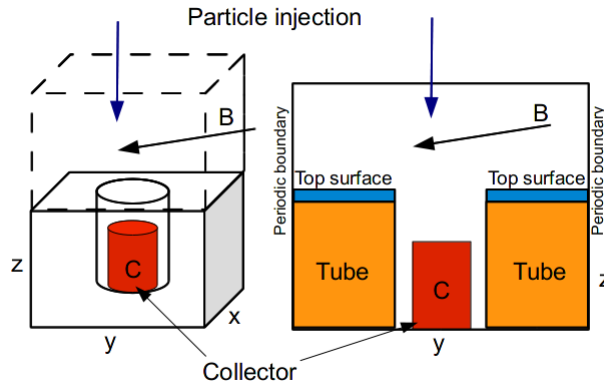


Figure 6.2: Schema of the SPICE3 simulation box for the Katsumata probe modeling. 3D view on the left, cross-section on the right showing the collector position

6.2.2 Simulation scenario

The probe was simulated in plasma with parameters similar to conditions in the tokamak SOL for deuterium plasma with a characteristic ratio of ion and electron temperatures. Note that the choice of plasma parameters has great impact on the computational demands, which restricts the range of plasma conditions we were able to simulate. The plasma conditions read:

- Plasma density $n = 1 \times 10^{18} \text{ m}^{-3}$
- Ion temperature $T_i = 70 \text{ eV}$
- Electron temperature $T_e = 50 \text{ eV}$
- Magnetic field magnitude $B = 1.0 \text{ T}$
- Magnetic field inclination $\alpha = 10^\circ$.

6.3 Electron transport inside the tube

To study the behaviour of electrons in vicinity of the probe, a simulation with parameters $h = 1 \text{ mm}$, $V_T = -3 kT_e$ and $V_C = +3 kT_e$ was performed. The choice of the collector potential corresponds to the electron branch of the I-V characteristics. Despite the collector being in magnetic shadow and $h \gg r_{Le}$ the simulation revealed an electron current flowing to the collector. The ratio of electron to ion collector currents R has been defined as follows:

$$R = \frac{I_C^-}{I_C^+}. \quad (6.1)$$

The simulation yields $R = 700$ ($I_C^- = -28.1 \text{ mA}$), which demonstrates the inefficiency of electron shielding. The mechanism of electron transport is based on the existence of self-consistent electric fields. Since ions can more easily penetrate into the tube than electrons (due to their large Larmor radius), a positive space charge appears near the tube entrance, which results in a potential structure formation. Subsequent electric field E_x near tube entrance creates an $\mathbf{E} \times \mathbf{B}$ drift driving the electrons along the z axis inside the tube (as shown in Fig. 6.3). The presence of electrons inside the tube affects the potential structure, so the system is in self-consistent equilibrium. The electron stream is flowing along the border of the potential structure (see Fig. 6.4).

The situation becomes different when V_C is changed to $-3 kT_e$, equal to tube potential V_T . The ratio of currents drops to $R = 0.07$ ($I_C^- = -0.022$

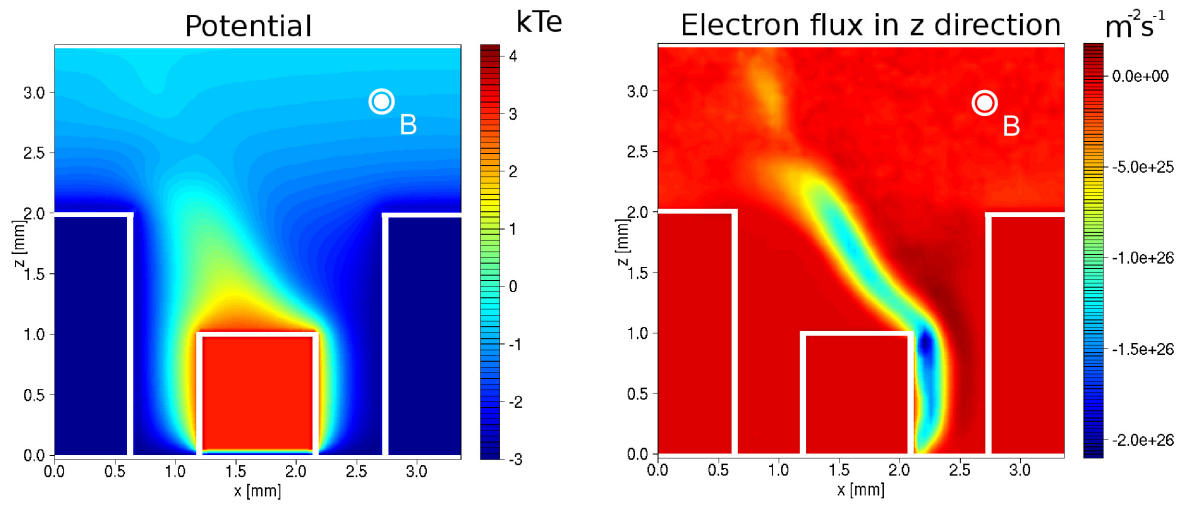


Figure 6.3: Vertical cross-section of the electric potential (left) and electron flux (right) at the tube axis for $V_T = -3kT_e$ and $V_C = +3kT_e$. Surfaces of objects have been highlighted.

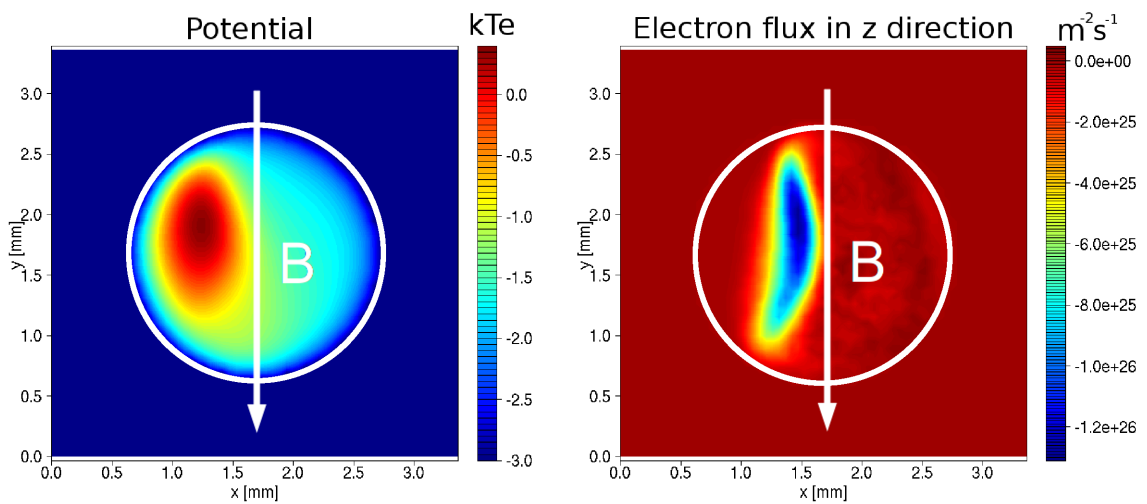


Figure 6.4: Horizontal cross-section of the electric potential (left) and electron flux (right) at the top surface. Negative flux shows electron flowing inside the tube.

mA), while for a regular Langmuir probe at floating potential R should be equal to one. This is in good agreement with experiment [54]. Electrons are still present in the tube (Fig 6.5), however they do not flow onto the collector but return to the plasma.

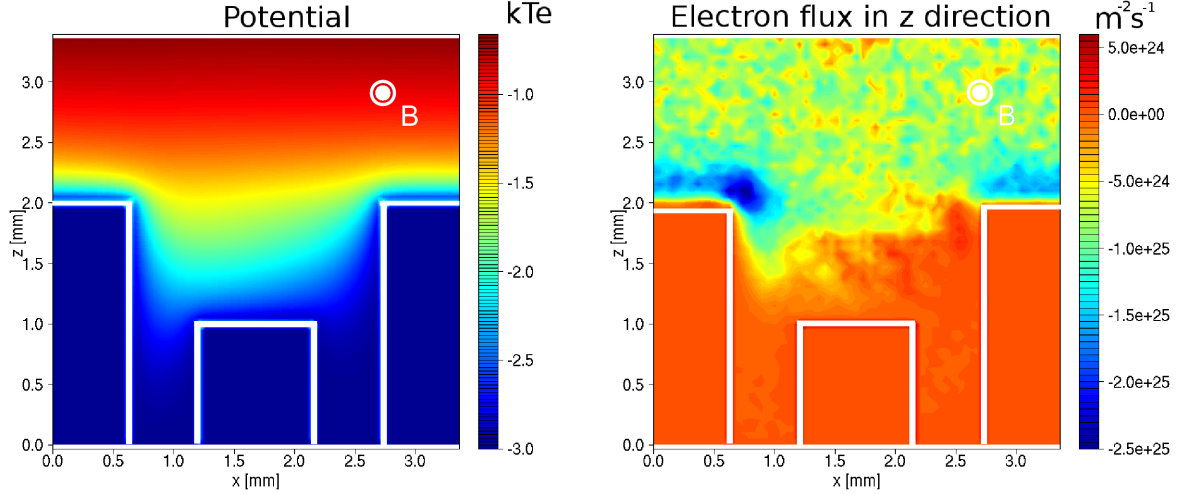


Figure 6.5: Vertical cross-section of the electric potential (left) and electron flux (right) at the tube axis for $V_T = -3 kT_e$ and $V_C = -3 kT_e$. Surfaces of objects have been highlighted.

6.3.1 Ion temperature estimation

In order to estimate ion temperature, it is necessary to sweep the collector voltage and record the I-V characteristics of the probe. The tube voltage has to be swept at the same time to enable electron shielding [33]. The ion branch of the characteristics can be then fitted by the formula

$$I_C \sim \exp\left(\frac{V_C}{T_i}\right) \quad (6.2)$$

The simulated I-V characteristics is shown in Fig. 6.6. The total collector current is in black, while the electron current in dashed blue. The electron current is largely suppressed (comparing to Langmuir probe, where it exceeds ion current for positive bias) allowing to fit the decay of ion current and to obtain estimate of ion temperature. The obtained temperature is 68 eV, which is in good agreement with the perpendicular temperature of injected particles (70 eV).

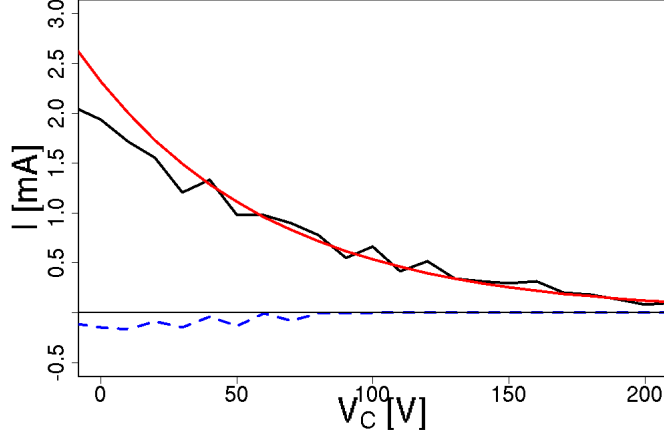


Figure 6.6: I-V characteristics of the Katsumata probe. Total current in black, electron current in blue. Fit for T_i estimation in red.

6.4 Mechanism of electron shielding

Based on the plasma behaviour observed in simulations, it is possible to explain the mechanism of electron shielding. The electrons are always present in the plasma shadow, which indicates that the transport is not limited by probe geometry but driven by $\mathbf{E} \times \mathbf{B}$ drift created by the potential structure, that appears near the tube entrance. Electrons have a vertical component of velocity along electrical equipotentials (see Fig. 6.7). When the collector is at the same potential as the tube, the equipotentials of the structure are separated from electrodes and electrons which enter the tube can leave it without contributing to the collector current. When the potentials are different, the collector may be connected to an equipotential which extends to plasma. In this case electrons propagating along such equipotential contribute to the collector current.

6.4.1 Role of magnetic field inclination

The simulated model differs from real diagnostics in the magnetic field orientation - the modeled tube axis is not perpendicular to the magnetic field lines but has an misalignment of 10 degrees, which is required by the numerical model. To clarify the role of such misalignment on the simulation results, two additional simulations were performed, both with $V_C = +3 kT_e$ and V_T

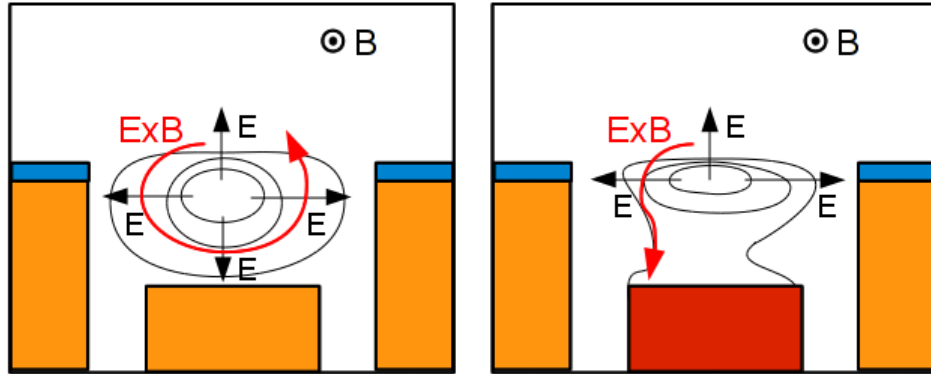


Figure 6.7: The role of $\mathbf{E} \times \mathbf{B}$ drift in case when $V_C = V_T$ (left) and $V_C \neq V_T$ (right)

$= -3 kT_e$. The misalignment has been changed to 5 and 2.5 degrees respectively. The later is already comparable to the misalignment of real probes. The electron collector current was reduced in magnitude to -7.76 and -2.54 mA respectively, however the simulations demonstrated, that the $\mathbf{E} \times \mathbf{B}$ drift transport mechanism is valid even for small misalignments.

6.5 Summary of the Katsumata probe simulations

A model of a Katsumata probe has been investigated. Electron transport into the probe tube has been confirmed and its origin attributed to the $\mathbf{E} \times \mathbf{B}$ drift along equipotential surfaces around a positive space charge structure due to gyration of ions into the mouth of the probe. Electron current suppression is observed when the collector and tube potentials are equal. In these conditions an exponential fit to the simulated I-V characteristics gives the correct ion temperature. Explanation of the electron current suppression has been derived. Simulations clarifying the role of magnetic field misalignment were performed and verified, that the transport mechanism is present even for small misalignments relevant to experimental conditions. The results could only be obtained thanks to the existence of fast 3D3V simulations.

Chapter 7

Simulations of gap crossings

7.1 Introduction

The gap simulations are interesting because of the implications for ITER and other next step devices. The gaps set operational limits to the machine because of fuel retention (especially when carbon is present inside the machine) and because of elevated heat fluxes, which occur on gap edges. In this chapter we shall focus on the later problem. The simulations of heat fluxes for ITER tiles have already been performed using the 2D code SPICE2 [37], however such simulations assume infinite length of the gaps. Real PFCs have finite dimensions and their gaps intersect in crossings. The crossings are expected to influence the plasma behaviour because of a combination of plasma flows. This interplay may result in a formation of a hotspot with elevated heat flux. In order to investigate such problem, a full 3D simulation is needed. The results will be compared to previous 2D simulations to validate the infinite gap assumption. The content of this chapter was presented at the 38th EPS conference and will be published in *Plasma Physics and Controlled Fusion*.

7.2 Geometry of the simulations

The simulation scenario has the same basic geometry setup as described in 6.2.1. The simulation region contains 4 blocks, which represent 4 corners of tiles and form a crossing of a poloidal gap (PG) and toroidal gap (TG) as shown in Fig. 7.1. The tiles are numbered 1-4 and the gaps are named to facilitate readers orientation in figures present in this chapter - poloidal left (PL), poloidal right (PR), toroidal bottom (TB) and toroidal top (TT). Due to computational constraints on the size of the region, only a part of a tile is simulated in the vicinity of the crossing. All blocks are kept at floating

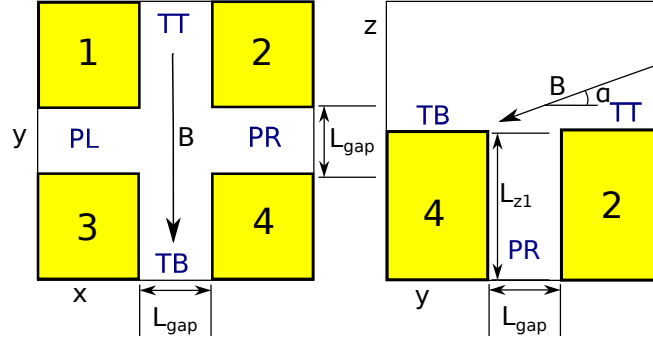


Figure 7.1: Schematic view of the gap crossing, top view (left) and side view (right).

potential. The magnetic field is parallel to the toroidal gap and has a given inclination α with respect to the tile top surface.

In order to investigate physical processes related to plasma interaction with the crossing, an example simulation with parameters relevant to SOL plasma conditions was performed. The plasma conditions were as follows:

- Plasma density $n = 2 \times 10^{18} \text{ m}^{-3}$
- Ion temperature $T_i = 50 \text{ eV}$
- Electron temperature $T_e = 25 \text{ eV}$
- Magnetic field magnitude $B = 2.0 \text{ T}$
- Magnetic field inclination $\alpha = 10^\circ$
- Ion Larmor radius $r_L = 0.72 \text{ mm}$
- Gap width $L_{gap} = 0.5 \text{ mm}$
- Gap depth $L_{z1} = 1.0 \text{ mm}$.

Note that these parameters are realistic for contemporary tokamak SOL, however far from expected ITER conditions, where the plasma density and magnetic field strength will be much higher. The available space of plasma parameters is severely restricted by computational demands. However, the key parameter, the ratio of ion Larmor radius to gap width, is kept the same as expected in ITER - of the order of unity. The aim of this simulation is to demonstrate transport mechanism related to the presence of gap crossing, not to predict exact values of heat fluxes on ITER divertor tiles. The results

can be compared to 2D simulations and used to correct the 2D simulations of the real plasma conditions.

7.3 Results of simulations

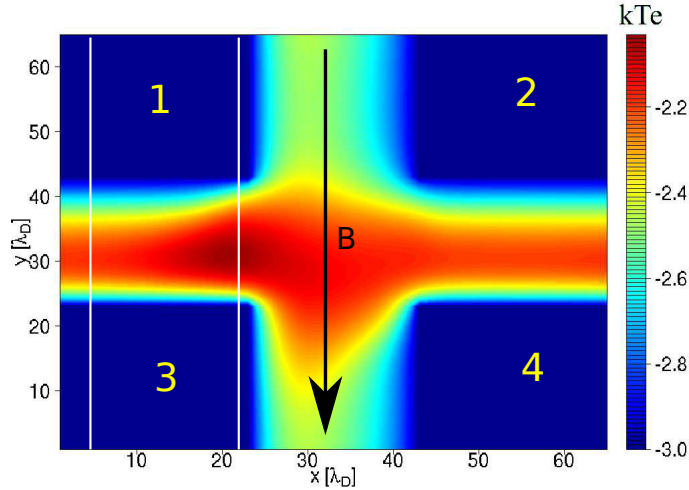


Figure 7.2: Top view of the normalized potential distribution inside the gap crossing at top tile surface. White lines show the cuts at $x=4$ (far from the crossing) and $x=22$ (close to the crossing).

The top view of the potential distribution at the top surface ($z = 50$) inside the gaps can be seen in Fig. 7.2. The potential shows an asymmetry in the vicinity of the crossing, which indicates that the crossing influences the plasma behaviour inside the gaps. Comparison of the potential profiles in 3D and 2D simulations inside the poloidal gap is shown in Fig. 7.3. The 3D simulation profile is taken far from the gap crossing ($x = 4$) in order to have the same conditions as the semi-infinite 2D simulation. The comparison shows that the potential peak is largely suppressed in the 3D simulation. The potential peak is in general a result of a positive space charge in magnetic shadow close to the gap entrance. In the case of an infinite gap, the area inside the shadow is perfectly screened from electrons (the model does not contain any mechanism of cross-field diffusion). The results of the 3D simulation show that electrons are present inside the gap (see Fig. 7.4). The presence of the electrons reduces the positive space charge and suppresses the potential structure near gap entrance.

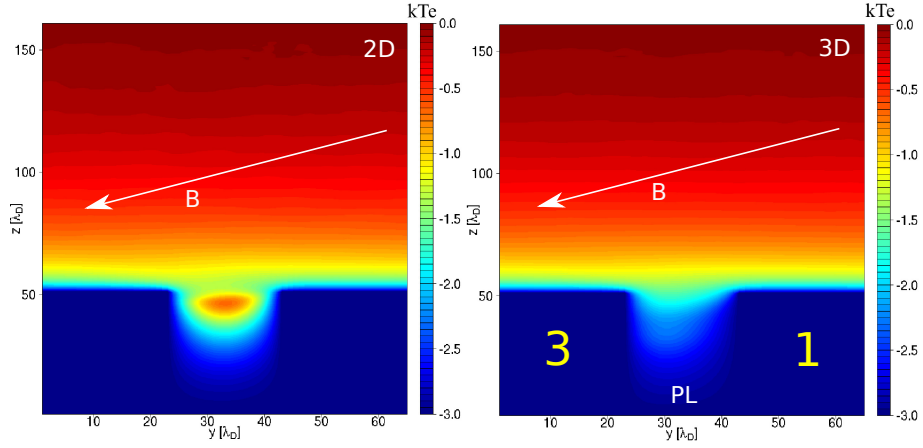


Figure 7.3: Comparison of the normalized potential distribution at the vicinity of the poloidal gap calculated by a 2D simulation (left) and a 3D simulation (right). The potential from the 3D simulation has been taken far from the gap at $x = 4$.

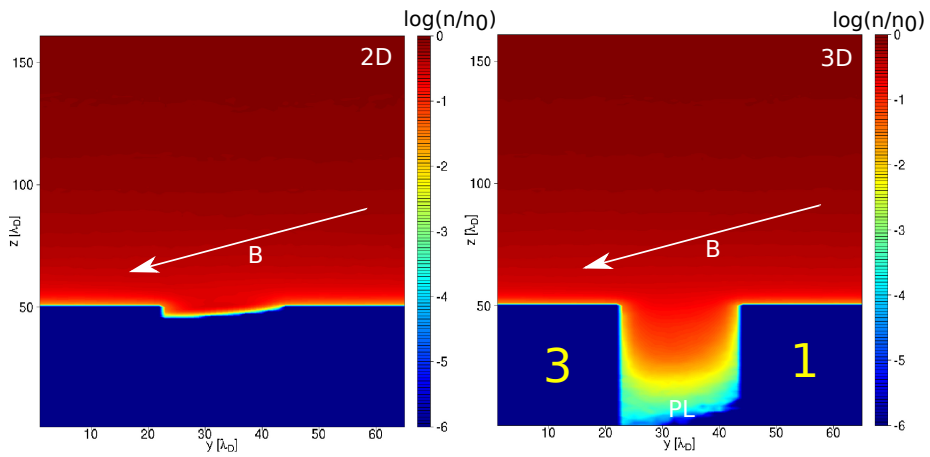


Figure 7.4: Comparison of the electron density at the vicinity of the poloidal gap calculated by a 2D simulation (left) and a 3D simulation (right). The density is normalized to plasma density and shown in a logarithmic scale. The potential from the 3D simulation has been taken far from the gap at $x = 4$.

Simulations show that the electrons can leak into the poloidal gap via the crossing. A fraction of electrons which enter a toroidal gap interact with the potential structure formed in the crossing and are pushed by an $\mathbf{E} \times \mathbf{B}$ drift inside the poloidal gap. Such electrons exhibit a complex set of motions. To illustrate the problem, we have represented one schematic trajectory in Fig. 7.5. The fastest motion is the Larmor gyro rotation (not shown in Fig. 7.5 due to the scale of the figure). Since the tiles are at floating potential, the electrons don't have enough energy to hit the tiles and recombine but they bounce between gap sides. The slowest motion is due to the $\mathbf{E} \times \mathbf{B}$ drift, which pushes them through the poloidal gap (to the left in Fig. 7.5). This way they can leak through the entire gap independently from its length and escape at the next crossing back into the toroidal gap. This mechanism thus changes the plasma interaction with the entire poloidal gap. It is a novelty, which can be only observed in a full 3D simulation.

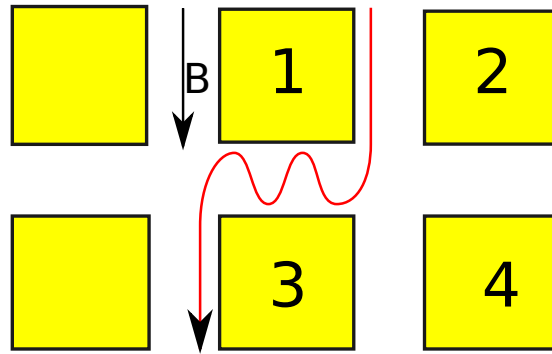


Figure 7.5: Trajectory of an electron coming from the a toroidal gap and leaking into the poloidal gap.

7.4 Maximum of the power flux

One of the applications of the PIC simulations of divertor tiles is to predict heat fluxes falling onto the tile surfaces. As shown in the previous section, the crossing perturbs the plasma behaviour and therefore the 3D profiles are different to those calculated in 2D. The goal of this section is to investigate its influence on the heat fluxes in the vicinity of the gap. Fig. 7.6 shows the power flux hitting the top tile surface. The variation of the flux across the surface is not very pronounced, however the top left corner of the crossing receives a flux increased by 20% comparing to the rest of the surface. Figures 7.7 and 7.8 show the power fluxes falling onto the gap sides in the poloidal

and toroidal gap. In each gap, there is a preferred side, where the majority of power flux is deposited. In case of PG, the power flux is deposited on the plasma wetted side, while in TG, there is one side preferred due to the direction of ion gyro rotation. The place with the largest power flux (0.55 MW/m^2) is located on the plasma wetted side of PG close to the gap crossing. This maximum is the same as observed in the 2D simulations. This does not mean that the heat flux distribution remains unchanged irrespective of the presence of the gap crossing. Figures 7.7 and 7.8 show that the fluxes are higher close to the crossing than further away. Rather than the peak value of the heat flux, we can calculate the integrated heat flux received along the gap on fixed x coordinate (in case of a poloidal gap).

$$Q_z(x_A, y_A) = \int_0^{Lz_1} \Gamma(x_A, y_A, z) dz, \quad (7.1)$$

where Lz_1 denotes the z coordinate of the tile top surface and (x_A, y_A) are the coordinates where we measure the power flux. The 2D simulation yields $Q_z = 4.68 \text{ MW/m}$, while the 3D simulation shows variation on the plasma-wetted side of PL between 6.3 (far away from the crossing) and 8.3 MW/m (close to the crossing), which is increase by 35% and 77% respectively. This is an important difference, as the integrated power flux will have an effect on the tile temperature.

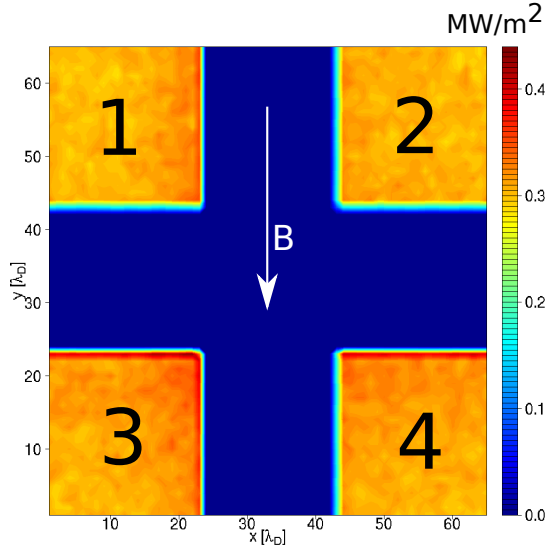


Figure 7.6: Power flux falling onto the top surface of the tile.

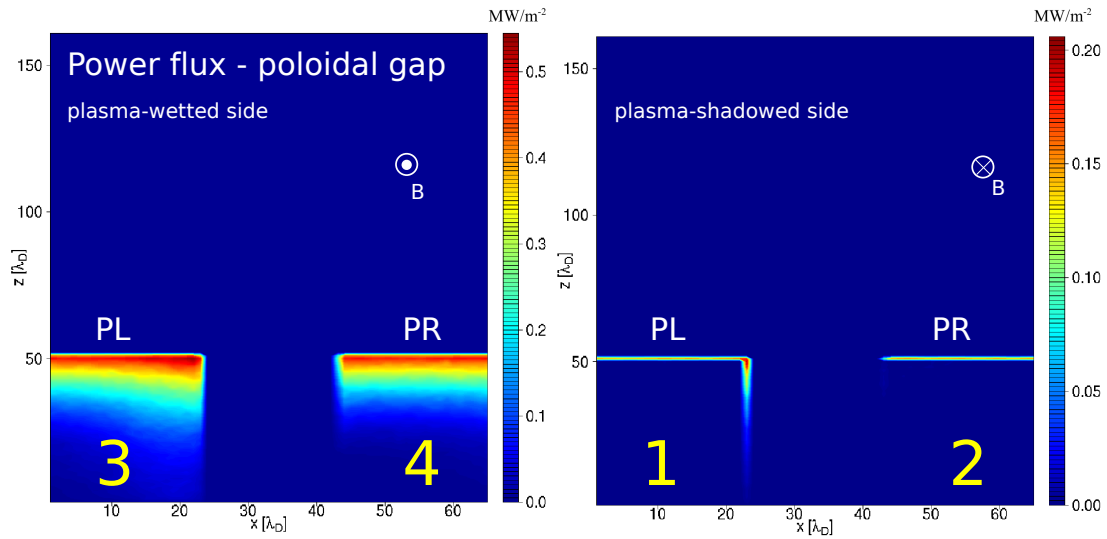


Figure 7.7: Power flux falling onto the plasma wetted side (left) and plasma shadowed side (right) of the poloidal gap.

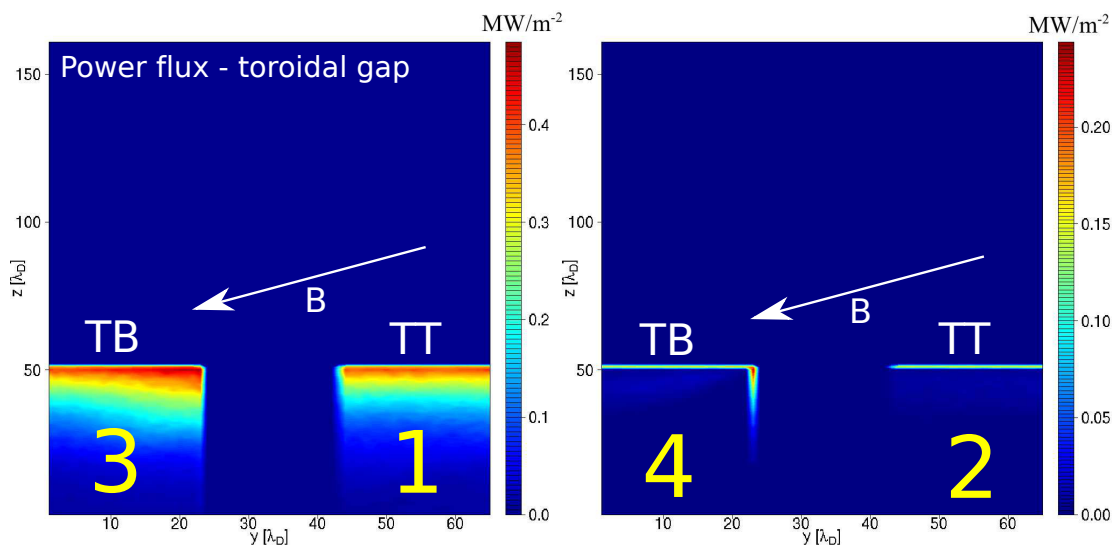


Figure 7.8: Power flux falling onto the left side (left) and right side (right) of the toroidal gap.

The disappearance of the potential structure indicates that the potential-dominated regime observed in 2D simulations does not occur and ions are no longer blocked from penetrating deep inside the gap. The comparison of ion heat deposition profiles (Fig. 7.9) demonstrates this effect - the ions penetrate deeper inside the gap in the 3D case and the total power flux deposited along the plasma wetted side is larger than in the 2D case. This indicates, that the 2D simulations are valid for conditions, where the gaps are in geometry-dominated regime. In this regime, the ion deposition is governed by the gap geometry and the potential peak is reduced. This has been typically the case for ITER simulations [37].

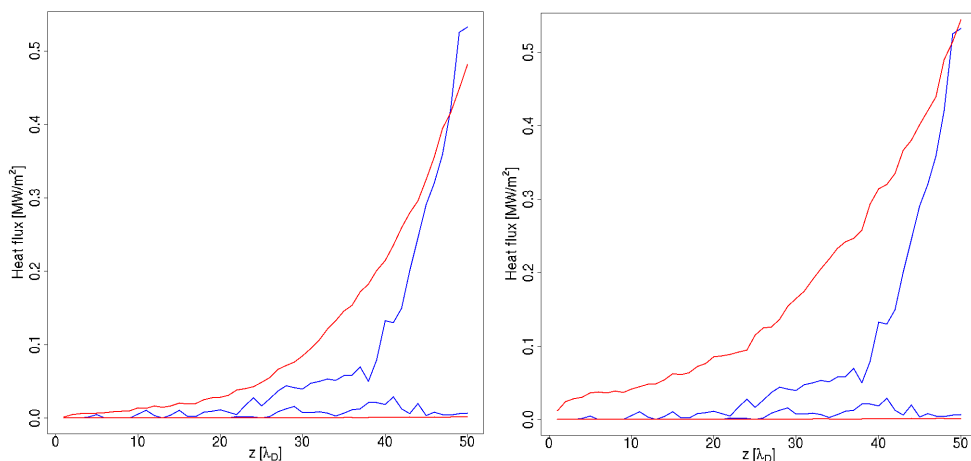


Figure 7.9: Power flux profiles inside the poloidal gap far from the crossing(left) and close to the crossing (right). The red curve shows 3D simulation, blue curve 2D simulation.

7.5 Summary of the 3D simulations of gap crossings

The new 3D3V simulations revealed new phenomena in the plasma interaction with the divertor tiles, which could not be modeled by a 2D code. The new mechanism observed is the electron leakage inside the poloidal gaps. The electrons coming from a TG are driven inside the PG by an $\mathbf{E} \times \mathbf{B}$ drift, which enables them to travel through the entire gap. The effect of the gap crossing is therefore non-local. The main consequence is that the electrons reduce the potential peak near the gap entrance, which changes the gap

regime from potential-dominated to geometry-dominated and influences the ion penetration inside the gap. As a result, the integrated power flux inside the poloidal gap is higher than predicted by a 2D simulation. The maximum increase of power flux is located on the plasma-wetted side of a poloidal gap close to the gap crossing, approximately twice the value obtained by a 2D simulation. All these results are only valid for a case where the toroidal gaps are perfectly aligned to the magnetic field and so the electrons can freely enter the toroidal gaps.

The simulations presented in this work are only a first step in the understanding of the underlying physics, used to demonstrate the new phenomena. Future studies will further develop this problematics, trying to perform simulations for ITER realistic conditions. There will be also studies of scenarios, where the toroidal gaps are not perfectly aligned with the magnetic field and so the electrons have limited access inside them. The resulting modification of the heat deposition patterns could be useful for the design of ITER divertor, enhancing the life time of the tiles.

Chapter 8

General conclusions

The Particle-In-Cell method has proven to be a useful technique for investigation of plasma interaction with solid objects in the Scrape-off Layer. The PIC can perform predictive modeling of high importance for the design of future fusion machines where other modeling methods cannot be used due to presumptions which are not satisfied in the sheath. A disadvantage of the method is a high demand on computational power. Therefore, the simulations are restricted to a small volume and there is a limited region of plasma parameters, which can be simulated.

The problems presented in this work are a subject of intensive research for a number of years. Although each part focuses on a different physical phenomena, they are all bound by the use of the same modelling method and the focus on ITER relevant issues.

Using our SPICE codes, we were able to investigate the plasma interactions with gaps in plasma-facing components. We have identified the main factors influencing the distribution of ion fluxes inside the gaps, which is of high importance for studies of fuel retention mechanisms. We have studied the effects of tile shaping, which reduces the amount of retained fuel inside the gaps. The results of the PIC simulations are, consequently, used as input of the neutral transport code 3D-GAPS, a tool to simulate the fuel retention. The simulations of gaps in TEXTOR test-limiter presented in this work provided basic understanding of the processes related to the tile shaping. The results of these simulations will be published in [55]. Future studies of this topic will focus on ITER-like geometry and plasma conditions to evaluate its applicability for ITER. The ultimate goal of this research is to find a configuration of tiles, which would enable the use of carbon in the tritium phase of ITER operation. This is highly desirable from the operational point of view due to a lack of experience with high-performance discharges in full-metal tokamaks.

The simulations of probes represent another area, where PIC simulations can be applied. Our model of the routinely used Katsumata probe for ion temperature measurements considerably contributed to the explanation of the underlying probe physics and its performance. Contrary to the model used in literature, we have shown that the probe does not rely on the difference between Larmor radii of ions and electrons. The shielding of electrons is achieved by a combination of potential peak formed close to the tube entrance and the potential of the electrodes. The new model of the probe agrees with experimental observations, which could not be explained before. The results were published in [49].

The prediction of heat fluxes on ITER PFCs is an important step towards the design of such components. The engineering limits of the tiles must not be exceeded, otherwise the life time of the tiles would be dramatically shortened. The 3D simulations of gap crossings have shown that there is a hotspot located close to one of the tile corners, which receives 1.7 times more of integral flux than what was predicted by a 2D simulation. These results will be published in [56]. The effects caused by a finite geometry of the gaps will be a subject of our future research. The aim will be to simulate realistic plasma conditions and couple the code with a heat equation solver, which would show the tile temperature.

The work presented in this thesis contributes to a better understanding of the underlying physics of plasma deposition inside the gaps between tiles. Moreover, the principle of a routinely used probe for ion temperature measurements has been explained thanks to our novel 3D simulations.

This thesis gives important contributions to the fusion community and the results presented here serve as useful inputs for further studies in the field of plasma wall interactions.

Acknowledgments

This work is a result of intensive collaboration between Institute of Plasma Physics CAS CR, v.v.i., Forschungszentrum Jülich and CEA Cadarache. It would be impossible to accomplish without devoted help of many people.

I express my gratitude to my thesis supervisor Dr. Renaud Dejarnac for guidance during the work and valuable recommendations concerning the text of the thesis.

Understanding of the TEXTOR test limiter experiments and modelling would be impossible without discussions with Dr. Andrey Litnovsky, Dr. Andreas Kirschner and Dr. Dmitry Borodin, as well as with Dr. Dmitry Matveev who spent lots of time explaining to me the functionality of the 3D-GAPS code and running impurity transport simulations.

I am grateful to Dr. James P. Gunn, co-author of the SPICE codes for helpful discussions concerning extension of the codes and problematics of the plasma sheath.

I would like to thank Mgr. Jiri Adamek, PhD. and RNDr. Jan Stockel, CSc. for inspiring discussions concerning the ion sensitive probes.

The simulations presented in this work could not be achieved without an important contribution of Mgr. Zdenek Pekarek, who provided us with the Poisson solvers.

I would like to thank my thesis director doc. Dr. Pavel Kudrna and thesis supervisor RNDr. Radomir Panek PhD., for smooth organization of my PhD.

Bibliography

- [1] J. Ongena and G. Van Oost. *Trans. Fusion Sc. Tech.*, (53), 2008.
- [2] J.A.Wesson. *Tokamaks*. Oxford University Press, 1987.
- [3] F.F. Chen. *Introduction to Plasma Physics*. Plenum Press, 1974.
- [4] F. Romanelli et al. *Fus. eng. and design*. (150-160, 84), 2009.
- [5] <http://www.iter.org>. Iter project.
- [6] V. Svoboda et al. *Fus. eng. and design*. (Article in Press), 2011.
- [7] V. Weinzettl et al. *Fus. eng. and design*. (Article in press), 2011.
- [8] A. Pospieszczyk et al. *J. of nucl. mat.* (947-952, 290-293), 2001.
- [9] R. Neu et al. *J. of nucl. mat.* (116-126, 313-316), 2003.
- [10] J. Pamela. *Fus. eng. and design*. (313-322, 46), 1999.
- [11] P.I. Pietersen. *Fus. eng. and design*. (171-177, 74), 2005.
- [12] V. Naulin. *J. of Nucl. Mat*, (363-365), 2007.
- [13] B. Pegourie et al. *J. of Nucl. Mat.*, 390–391:550–555, 2009.
- [14] E.M. Hollmann. *Phys. of plasmas*. (9), 2002.
- [15] M. J. Rubel et al. *Phys. Scr.*, (112-117), 2004.
- [16] C.H. Skinner. *Nucl. Fusion*, (271), 1999.
- [17] J. Roth et al. *J. of Nucl. Mat.*, (390-391), 2009.
- [18] E. Salonen et al. *J. of Nucl. Mat*, (144-147, 290-293), 2001.
- [19] A.A. Haasz. *J. of Nucl. Mat.*, (85-88), 2001.

- [20] F.L. Tabares. *J. of nucl. mat.* (839-844), 2003.
- [21] R. Dux et al. *J. of Nucl. Mat.*, (390-391), 2009.
- [22] A. Litnovsky et al. *J. of Nucl. Mat.*, (390-391), 2009.
- [23] A. Litnovsky et al. *J. of Nucl. Mat.*, (367-370), 2007.
- [24] A. Litnovsky et al. *J. of Nucl. Mat.*, (809-812), 2009.
- [25] D. Matveev. *Modeling of material deposition in the gaps of castellated surfaces in fusion experiments.* diploma thesis, 2009.
- [26] R. Dejarnac, **M. Komm**, J. Stockel, and R. Panek. *J. of Nucl. Mat.*, (382), 2008.
- [27] S.E. Pestchanyi. *Fus. Eng. and Design*, (1657-1663), 2007.
- [28] M. Kocan et al. *J. of nucl. mat.* (Article in press), 2010.
- [29] M. Kocan et al. *J. of nucl. mat.* (363-365), 2007.
- [30] A. S. Wan et al. *Rev. sci. instrum.* (1542), 1986.
- [31] I. Katsumata. *Contrib. plasma phys.* (365), 1996.
- [32] S.V. Ratynskaia. *Rev. sci. instrum.* (73), 2002.
- [33] J. Adamek et al. *Contrib. plasma phys.* (48), 2008.
- [34] R. Chodura. *Phys. Fluids*, 25, 1982.
- [35] C.K. Birdsall and A.B. Langdon. *Plasma Physics via Computer Simulation.* McGraw-Hill, New York, 1985.
- [36] Y. Idomura et al. *Comp. Phys. Comm.*, (179), 2008.
- [37] R. Dejarnac, **M. Komm**, J.P. Gunn, and R. Panek. *J. of Nucl. Mat.*, (390-391), 2009.
- [38] R. Dejarnac, **M. Komm**, J.P. Gunn, and R. Panek. *J. nucl. mat.* (818-821), 2009.
- [39] J.P. Gunn. *J. of nucl. mat.* (337-339), 2005.
- [40] O. Buneman. *J. Comput. Phys.*, 1:517, 1967.

- [41] H. William et al. *Numerical Recipes in Fortran*. Cambridge University Press.
- [42] T. A. Davis. *Acm trans. on math. software.* (30), 2004.
- [43] <http://www.tacc.utexas.edu/resources/software/#blas>. Gotoblas library.
- [44] <http://www.open-mpi.org>. Openmpi library.
- [45] <http://spice2.sourceforge.net>. Spice2 homepage.
- [46] R.Dejarnac and J.P. Gunn. *J. of nucl mat.* (363-365), 2007.
- [47] D. Matveev, A. Kirschner, A. Litnovsky, **M. Komm**, D. Borodin, V. Philipps, and G. van Oost. *Plasma Phys. Control. Fusion*, (52), 2010.
- [48] W. Hackbusch. *Multi-grid methods and applications*. Springer, 1985.
- [49] **M. Komm**, J. Adamek, R. Dejarnac, J. P. Gunn, and Z. Pekarek. *Plasma phys. control. fus.* (53), 2011.
- [50] L.H. Hutchinson. *Principles of Plasma Diagnostics (2nd ed.)*. Cambridge University Press, 2002.
- [51] J. Adamek et al. *Czech. j. phys.* (54), 2004.
- [52] J. Adamek et al. *J. of nucl. mat.* (390-391), 2009.
- [53] J. Adamek et al. *Czech. j. phys.* (55), 2005.
- [54] N. Ezumi. *Contrib. plasma phys.* (41), 2002.
- [55] **M. Komm**, R. Dejarnac, J.P. Gunn, A. Litnovsky, D. Matveev, A. Kirschner, and Z. Pekarek. submitted to *plasma phys. control. fus.* 2011.
- [56] **M. Komm**, R. Dejarnac, J. Horacek, J.P. Gunn, and Z. Pekarek. submitted to *plasma phys. control. fus.* 2011.